

Terahertz Polaritonics

T. Feurer,¹ Nikolay S. Stoyanov,²
David W. Ward,² Joshua C. Vaughan,²
Eric R. Statz,² and Keith A. Nelson²

¹Institute for Applied Physics, 3012 Bern, Switzerland

²Department of Chemistry, Massachusetts Institute of Technology, Cambridge, Massachusetts 02139; email: kanelson@mit.edu

Annu. Rev. Mater. Res. 2007. 37:317–50

First published online as a Review in Advance on
March 27, 2007

The *Annual Review of Materials Research* is online at
<http://matsci.annualreviews.org>

This article's doi:
10.1146/annurev.matsci.37.052506.084327

Copyright © 2007 by Annual Reviews.
All rights reserved

1531-7331/07/0804-0317\$20.00

Key Words

THz technology, ultrafast spectroscopy, femtosecond pulse
shaping, ferroelectrics, lattice dynamics, phonon-polaritons

Abstract

Between electronics and photonics there exists a frequency gap of approximately two octaves, i.e., the frequency range between 100 GHz and 10 THz, across which there are limited capabilities for signal generation, control, guidance, and processing. Here, we demonstrate that phonon-polaritons in ionic crystals like LiNbO₃ or LiTaO₃ may be used to bridge this gap. The ability to directly visualize polariton fields through real-space imaging, to generate arbitrary THz waveforms through the use of temporally and/or spatially shaped optical waveforms, and to fabricate integrated functional elements for polariton guidance and control through laser machining yields a THz polaritonics platform that enables advanced signal processing and spectroscopy applications.

INTRODUCTION

The terahertz (THz) gap between high-frequency electronics (up to roughly 100 GHz) and low-frequency optics (down to roughly 10 THz) has recently gained intense interest in connection with a wide range of applications, including high-bandwidth signal processing, THz imaging, and THz spectroscopy (1–7). The applications have been spurred by the emergence of femtosecond laser-based methods for the generation of THz pulses (1–19). However, none of these methods have provided a versatile platform for complex THz waveform generation, guidance, processing, and characterization. Such a platform could find applications in both THz signal processing and spectroscopy.

Here we review the foundational work in the area of THz polaritonics, in which the signal carriers are neither AC electric currents nor pure electromagnetic waves but phonon-polaritons, strongly coupled admixtures between electromagnetic waves and polar lattice vibrations of comparable frequency and wavevector (20, 21). In the polaritonics platform, coherent THz signals are generated by femtosecond optical pulses through impulsive stimulated Raman scattering (ISRS) (12, 22–26), a second-order nonlinear optical process. This requires that the phonon-polariton modes involved be both Raman and infrared active and therefore that the host crystal be noncentrosymmetric. In addition, the THz signals do not propagate collinearly with the optical beams that generate them, as they would in the case of phase-matched or quasi-phase-matched signal generation (13–17). Instead, they propagate primarily in lateral directions, with the largest wavevector components perpendicular to the optical beam path (12, 26, 27). This key property, which enables interactions of the THz signals with further optical pulses and with integrated structures, arises because the THz dielectric constant is extremely high, resulting in a refractive index that is substantially higher at THz than at optical frequencies. The material requirements point clearly toward ferroelectrics (28). Although the optimal substrate may remain to be discovered or fabricated, the developmental groundwork in polaritonics has been conducted with lithium tantalate and lithium niobate single crystals, whose combinations of strong Raman activity and electro-optic coefficients, high THz dielectric constants and moderate THz damping rates, and optical transparency facilitate polaritonics applications. Ferroelectric crystals, which for many years have found extensive applications as piezoelectric transducers and receivers of MHz-frequency acoustic waves, may find complementary roles as electro-optic transducers and receivers of GHz-THz-frequency polariton waves.

The Polaritonics Toolset

There are three primary components of the polaritonics toolset that distinguish it from more conventional THz methodology:

1. spatiotemporal imaging of polariton fields and their evolution (29–33),
2. spatiotemporal coherent control over polariton generation and propagation (34–37), and
3. integrated polaritonic functional elements, including waveguides, resonators, and more complex elements composed of them (38–43).

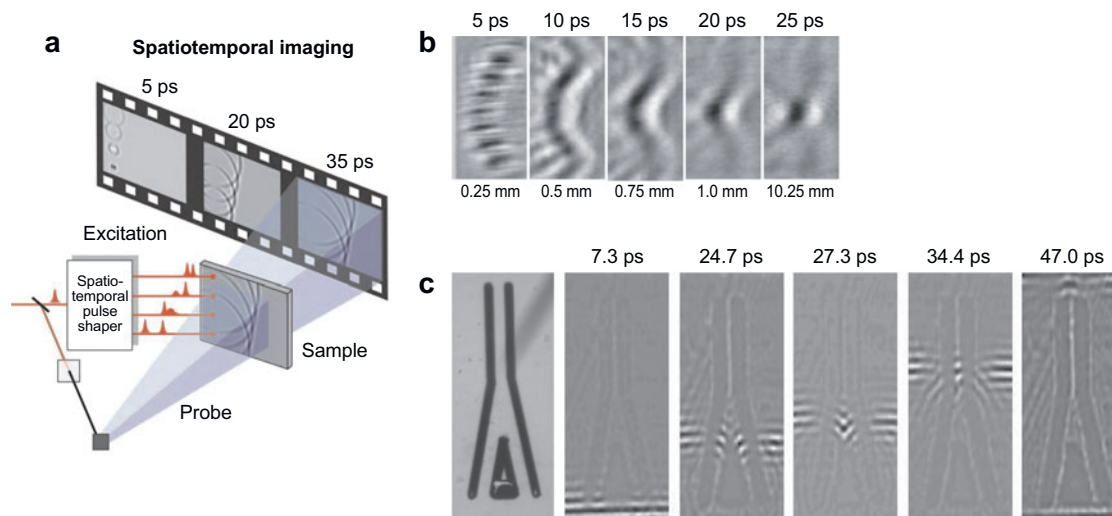


Figure 1

The polaritonics toolset. (a) Spatiotemporal coherent control and spatiotemporal imaging of THz polaritons. Spatiotemporal femtosecond pulse shaping is used for reconfigurable generation of specified time- and position-dependent optical excitation fields that generate correspondingly specified polariton fields. Real-space images of the polariton field are recorded at variable delays following excitation (adapted from Reference 36). (b) THz phased/timed array generation. Eight pulses arrive at distinct spots that are vertically arrayed, with a parabolic temporal sweep, generating a parabolic wavefront that focuses in the far field at a specified time and sample location, or “address.” The simulated images in *a* illustrate the generation of a tilted planar wavefront by four pulses with a linear temporal sweep. (c) An integrated waveguide Y-coupler and images of THz signals propagating within it. The structure was fabricated by femtosecond laser machining of air trenches (the black regions in the optical micrograph at the left) into a 500- μm -thick lithium niobate crystal. The unmachined crystalline regions (approximately 200 μm wide) between the air trenches act as polariton waveguides.

Figure 1 illustrates some features of these components. The essential elements of **Figure 1** are readily appreciated even prior to the technical elaboration that follows. In particular, the figure shows or suggests the following:

1. impulsive excitation of polaritons with femtosecond optical pulses,
2. primarily lateral polariton propagation relative to optical beam,
3. real-space- and real-time-resolved (i.e., spatiotemporal) polariton imaging,
4. coherent control over polariton responses through reconfigurable spatial and temporal (i.e., spatiotemporal) shaping of the optical fields that generate them,
5. single-cycle or multiple-cycle THz generation,
6. integrated THz functional elements,
7. linear signal processing through coherent superposition of THz signals, and
8. a solid-state platform for integrated THz wave generation, propagation, guidance, manipulation, and imaging/readout.

This review illustrates several additional features: (a) coupling of THz waves into free space or other adjacent media, (b) THz wave amplification through coherent

superposition, and (c) high attainable THz field amplitude, pulse energy, and average power.

The following section presents a brief theoretical description of polariton excitation, propagation, and detection/visualization and a short summary of phonon-polariton measurements prior to the development of the toolset components indicated above. This is followed by a discussion of experimental observations of polaritons under a wide range of excitation conditions in unpatterned and patterned materials. Finally, future directions for polaritonics and its applications are suggested.

BACKGROUND

Theoretical Description

When light at THz frequencies propagates through a transparent crystal, the electromagnetic field may couple to polar lattice vibrations (transverse optic phonon modes) of similar frequencies to form a phonon-polariton wave (20, 21). This section briefly describes phonon-polaritons and their excitation and detection with femtosecond optical pulses. Most of the considerations presented are general, but phonon-polariton properties in lithium niobate and lithium tantalate crystals are emphasized specifically.

Phonon-polariton modes. To treat light propagating through a nonmagnetic transparent crystal, we start with Maxwell's equations in the following form:

$$\nabla \times \mathbf{E}(\mathbf{r}, t) = -\mu_0 \frac{\partial \mathbf{H}(\mathbf{r}, t)}{\partial t}, \quad 1.$$

$$\nabla \times \mathbf{H}(\mathbf{r}, t) = \varepsilon_0 \frac{\partial \mathbf{E}(\mathbf{r}, t)}{\partial t} + \frac{\partial \mathbf{P}(\mathbf{r}, t)}{\partial t}, \quad 2.$$

$$\nabla \cdot [\varepsilon_0 \mathbf{E}(\mathbf{r}, t) + \mathbf{P}(\mathbf{r}, t)] = 0, \quad 3.$$

$$\nabla \cdot \mathbf{H}(\mathbf{r}, t) = 0. \quad 4.$$

The magnetization is zero, and there are neither currents nor free charges. To derive a relation between the polarization and the electric field, we assume that the crystal consists of independent harmonic oscillators (phonon modes) that couple to the electric field through their dipole moments. The equation of motion of the amplitude $\mathbf{Q}_k(\mathbf{r}, t)$ of a single oscillator k is

$$\frac{\partial^2 \mathbf{Q}_k(\mathbf{r}, t)}{\partial t^2} + \bar{\Gamma}_k \frac{\partial \mathbf{Q}_k(\mathbf{r}, t)}{\partial t} + \bar{\omega}_{Tk}^2 \mathbf{Q}_k(\mathbf{r}, t) = \sqrt{\varepsilon_0} \sqrt{f_k} \mathbf{E}(\mathbf{r}, t), \quad 5.$$

where $\bar{\Gamma}_k$ is a phenomenological damping constant, $\bar{\omega}_{Tk}$ the resonance frequency, and f_k the coupling or the oscillator strength. Fourier transforming to the frequency domain and collecting all modes leads to the dielectric tensor

$$\epsilon_{ij}(\omega) = 1 + \sum_k \frac{f_{ijk}}{\omega_{Tk}^2 - \omega^2 + i\Gamma_k \omega}. \quad 6.$$

LiNbO₃ and LiTaO₃ are both uniaxial crystals, and the three principal axes can be divided into two ordinary axes and one extraordinary axis. In the crystal's reference system, the tensors $\bar{\Gamma}_k$, $\bar{\omega}_{Tk}$, and \bar{f}_k are all of diagonal form. For frequencies below the lowest phonon resonance, usually only this resonance is of importance, and all other contributions are cast into a single constant ϵ_{∞} . The dielectric function is also diagonal, and the ordinary and extraordinary components ($\alpha = o, eo$) are

$$\epsilon_{\alpha}(\omega) = \epsilon_{\infty\alpha} + \frac{f_{\alpha}}{\omega_{T\alpha}^2 - \omega^2 + i\Gamma_{\alpha}\omega} = \epsilon_{\infty\alpha} + \frac{\omega_{T\alpha}^2(\epsilon_{0\alpha} - \epsilon_{\infty\alpha})}{\omega_{T\alpha}^2 - \omega^2 + i\Gamma_{\alpha}\omega}. \quad 7.$$

The oscillator strength can be determined from a measurement of the dielectric constant at zero frequency, i.e., $\epsilon_{0\alpha} = \epsilon_{\alpha}(0)$. **Table 1** lists the constants for LiNbO₃ and LiTaO₃ for ordinary and extraordinary polarized THz waves. The values in **Table 1** were derived from various sources (44–48), and different growth methods can yield considerable variation.

From the dielectric function we may derive the index of refraction $n_{\alpha}^2(\omega) = \epsilon_{\alpha}(\omega)$ and the dispersion diagram, as shown in **Figure 2**. The uncoupled photon and phonon dispersion curves eventually meet, and the coupling leads to an avoided crossing.

Table 1 Material constants and important properties^a

		LiNbO ₃		LiTaO ₃	
		o	eo	o	eo
Pump/probe	n (800 nm)	2.257	2.163	2.153	2.157
	n_g (800 nm)	2.358	2.250	2.231	2.236
	n (400 nm)	2.439	2.312	2.278	2.282
	n_g (400 nm)	3.050	2.800	2.617	2.619
THz	ϵ_0	41.5	26.0	41.5	37.6
	ϵ_{∞}	19.5	10.0	17.4	7.6
	$\omega_T/2\pi$ (THz)	4.6	7.4	4.3	6.0
	$\Gamma/2\pi$ (THz)	0.42	0.63	0.42	0.84
0.5 THz	n	6.46	5.11	6.47	6.15
	n_g	6.50	5.12	6.52	6.18
	Abs length $1/\alpha$ (mm)	2.7	5.3	2.2	1.7
	Critical angle (deg)	8.90	11.29	8.89	9.36
	Brewster angle (deg)	8.80	11.08	8.79	9.24
	Cherenkov angle (deg)	68.6	63.7	69.8	68.7
	Tilt angle (deg)	21.4	26.3	20.2	21.3
	Probe angle (deg)	14.7	14.6	7.8	8.2
Electro-optic	r_{13} (10 ¹² m V ⁻¹)		9.6		4.5
	r_{22} (10 ¹² m V ⁻¹)		6.8		0.3
	r_{33} (10 ¹² m V ⁻¹)		30.9		27
	r_{51} (10 ¹² m V ⁻¹)		21.1		15

^aSources: optical constants LiNbO₃ (44) and LiTaO₃ (45), THz properties LiNbO₃ (46) and LiTaO₃ (47), and electro-optic constants (48).

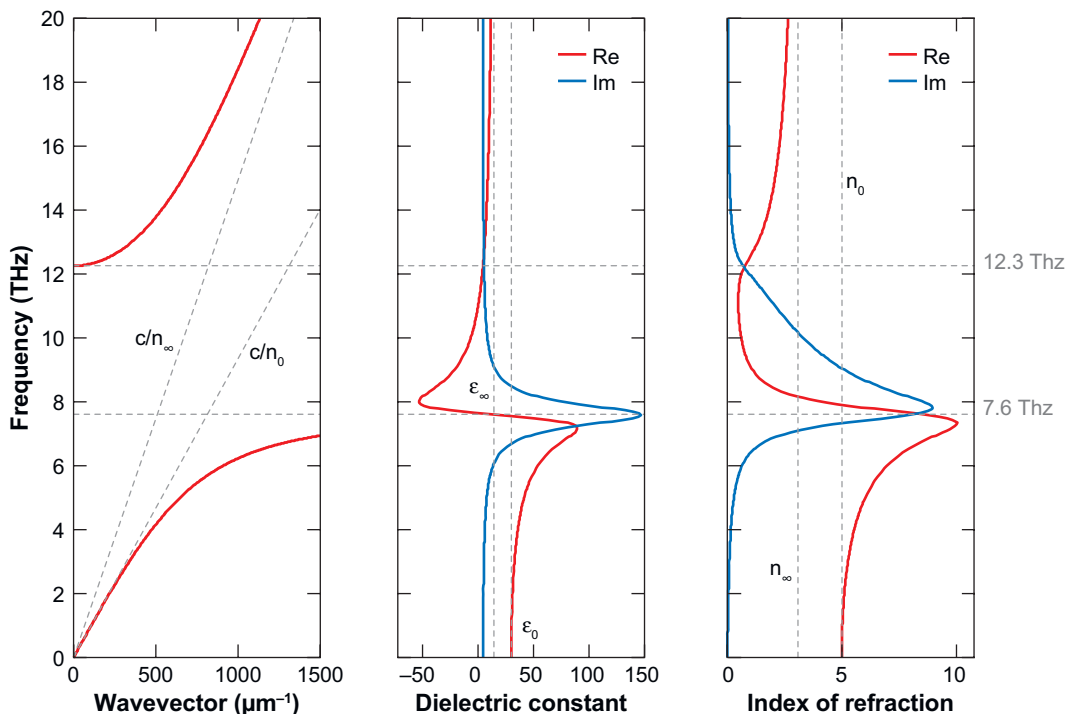


Figure 2

Dispersion relation, dielectric function, and index of refraction for LiNbO₃. The polarization is extraordinary, and we consider only the lowest-frequency optic phonon mode.

The lower branch is almost linear, i.e., light-like, for low frequencies and becomes nearly constant, i.e., phonon-like, for high frequencies. In this work we deal almost exclusively with frequencies below resonance in the nearly linear part of the dispersion relation.

With the dielectric function (7) derived from a simple oscillator model, it is possible to combine the equation of motion with Maxwell's equations in a set of four first-order differential equations, one set for each polarization, ordinary and extraordinary. Hereafter, we drop the index α .

$$\nabla \times \mathbf{E}(\mathbf{r}, t) = -\mu_0 \frac{\partial \mathbf{H}(\mathbf{r}, t)}{\partial t}, \quad 8.$$

$$\nabla \times \mathbf{H}(\mathbf{r}, t) = \varepsilon_0 \epsilon_\infty \frac{\partial \mathbf{E}(\mathbf{r}, t)}{\partial t} + \omega_T \sqrt{\varepsilon_0(\epsilon_0 - \epsilon_\infty)} \mathbf{V}(\mathbf{r}, t), \quad 9.$$

$$\frac{\partial \mathbf{V}(\mathbf{r}, t)}{\partial t} = -\Gamma \mathbf{V}(\mathbf{r}, t) - \omega_T^2 \mathbf{Q}(\mathbf{r}, t) + \omega_T \sqrt{\varepsilon_0(\epsilon_0 - \epsilon_\infty)} \mathbf{E}(\mathbf{r}, t), \quad 10.$$

$$\frac{\partial \mathbf{Q}(\mathbf{r}, t)}{\partial t} = \mathbf{V}(\mathbf{r}, t), \quad 11.$$

where ϵ_0 is the free space permittivity, distinct from ϵ_0 , the low-frequency crystalline dielectric constant, and $\mathbf{V}(\mathbf{r}, t)$ is the velocity of vibrational motion. The formulation of Equations 8–11 is especially useful for finite difference time domain simulation (49, 50) because first, numerical stability is usually better than for second-order differential equations and second, a spatially varying dielectric function is relatively easy to incorporate.

Excitation of polaritons through nonlinear optical effects. When an intense laser pulse passes through the medium, it creates a region of a nonlinear polarization that may act as a source term for the THz field $\mathbf{E}(\mathbf{r}, t)$ (12, 26). The nonlinear coupling can in principle be electronic or ionic in nature; that is, the driving laser transfers energy directly to either the electronic system or the phonon system.

$$\nabla^2 \mathbf{E}(\mathbf{r}, \omega) + \frac{\omega^2}{c^2} \epsilon(\omega) \mathbf{E}(\mathbf{r}, \omega) = -\frac{\omega^2}{c^2} \chi^{(2)} \mathcal{E}(\mathbf{r}, \omega) \otimes_{\omega} \mathcal{E}^*(\mathbf{r}, \omega), \quad 12.$$

where c is the speed of light in vacuum; $\chi^{(2)}$, the effective second-order nonlinearity, which includes electronic and ionic contributions; $\mathcal{E}(\mathbf{r}, \omega)$, the electric field of the driving laser pulse; and \otimes_{ω} , the convolution with respect to frequency. In the low-frequency limit, i.e., $\epsilon(\omega) \approx \epsilon_0$, the above equation is easily Fourier transformed to give

$$\nabla^2 \mathbf{E}(\mathbf{r}, t) - \frac{\epsilon_0}{c^2} \frac{\partial^2 \mathbf{E}(\mathbf{r}, t)}{\partial t^2} = \frac{1}{c^2} \chi^{(2)} \frac{\partial^2}{\partial t^2} |\mathcal{E}(\mathbf{r}, t)|^2. \quad 13.$$

This differential equation is formally solved by the Green's function method (26). **Figure 3** shows a typical geometry. A cylindrically focused laser pulse is polarized

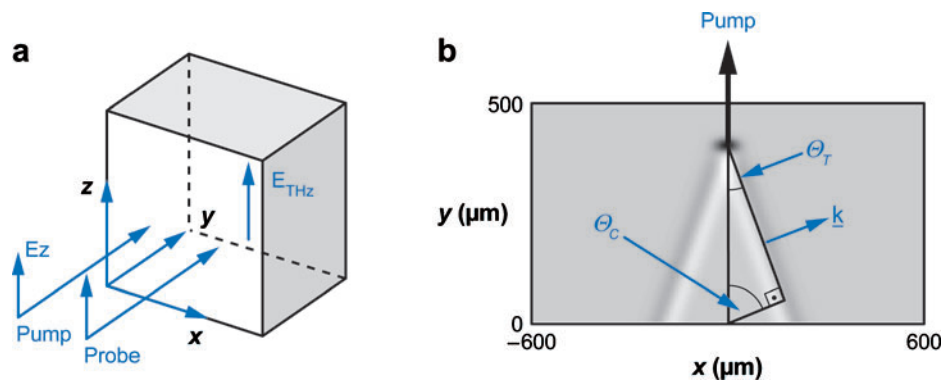


Figure 3

(a) Pump and probe fields propagate parallel to the y axis, and their polarizations as well as the optic axis are parallel to z . (b) Top view of polariton response to a cylindrically focused line source with a waist of 50 μm . The polariton electric field distribution is shown, with white corresponding to positive and black to negative field amplitudes. (The positive and negative polariton vibrational displacements also may be inferred because they are proportional to the field distribution.) The Cherenkov and tilt angles are indicated.

along the optic (z , or extraordinary) axis and drives a polariton plane wave response with the same polarization. If we assume that the excitation field is an infinitely tall line source with a Gaussian spatial profile of width w_0 in the horizontal (x) dimension and a Gaussian temporal profile of duration τ and that this source moves parallel to the y axis without changing its shape, then the polariton electric field is given by

$$E_z(x, y, t) \propto \frac{\partial}{\partial y} \int dx' e^{-2x'^2/w_0^2} \exp \left[-\frac{(y - v_g t + |x - x'| \tan \theta_C)^2}{v_g^2 \tau^2} \right], \quad 14.$$

where v_g is the group velocity of the driving laser pulse and θ_C the Cherenkov angle, with $\tan \theta_C = \sqrt{(nv_g/c)^2 - 1}$ and n the index of refraction at THz frequencies. The two-dimensional solution as shown in **Figure 3b** is a single-cycle plane wave propagating almost perpendicular to the propagation direction of the excitation pulse with a small forward component k_y . This forward component results from the finite speed of propagation v_g of the excitation pulse through the sample and the lower phase velocity of the generated polariton wave. When an 800-nm excitation pulse enters the sample, the polariton response generated near the front surface travels some measurable distance before the excitation pulse reaches the back of the sample and generates a polariton wavelet there. Because the radiation source moves faster than the phase velocity of the radiation generated, the THz field can be thought of as Cherenkov-type radiation, as indicated in **Figure 3b** (12, 26, 27). For LiNbO₃ the Cherenkov angle θ_C is large, approximately 64°. Frequently, we use the term tilt angle of the THz wavefront, which is given by $\theta_T = 90 - \theta_C$. Because of this slight forward component and the finite sample thickness, the polariton wave bounces back and forth, undergoing total internal reflection from the back and front faces of the sample as it progresses laterally.

For the geometry shown in **Figure 3b**, it is relatively straightforward to derive that the profile of the polariton wave along the x axis is proportional to the spatial derivative of the driving laser's transverse profile with respect to x (37). This fact is very useful, as it allows us to tailor the THz field simply by adjusting the spatial excitation profile accordingly. This relation is also useful for estimating the center frequency and the frequency content of the polariton wave. For a Gaussian pulse the maximum of the THz spectrum occurs at

$$f_{\max} \approx \frac{c}{\pi n w_0}. \quad 15.$$

Principles of polariton detection. Phonon-polaritons induce a change in the index of refraction at an optical probe wavelength, which is proportional to the lattice vibrational displacement and therefore to the THz electric field. Within the formalism of the electro-optic effect, the change of the index of refraction at visible wavelengths is given by (51)

$$\frac{1}{n_i^2} = \frac{1}{n_i^2} \bigg|_{E=0} + \sum_j r_{ij} E_j, \quad 16.$$

where the electro-optic tensor for a crystal with symmetry $3m$, such as LiNbO_3 or LiTaO_3 , is

$$\mathbf{r} = \begin{pmatrix} 0 & -r_{22} & r_{13} \\ 0 & r_{22} & r_{13} \\ 0 & 0 & r_{33} \\ 0 & r_{51} & 0 \\ r_{51} & 0 & 0 \\ -r_{22} & 0 & 0 \end{pmatrix} \quad 17.$$

with the usual contraction of indices. A THz field that is polarized along the optic axis, i.e., $i = 3$ and $n_3 = n_e$, causes an instantaneous phase modulation of a similarly polarized, y -propagating probe pulse given by

$$\mathcal{E}_z(x, z, t) = \mathcal{E}_{z0}(x, z, t) \exp \left[-i \frac{\omega}{c} \left(n_e - \frac{n_e^3}{2} r_{33} E_z(x, z, t) \right) y \right]. \quad 18.$$

The phase shift of the probe pulse, integrated through the crystal thickness, can be measured directly through interferometry or through induced birefringence or probe spectral shifts (the spectral shift is proportional to the time derivative of the index of refraction) (22, 52). We also have measured polariton-induced changes in second harmonic generation. Any of these measurements can be conducted with a localized probe beam focused to a selected spot of the crystal or with an expanded beam that is passed through the entire sample region of interest and transmitted to a CCD camera for real-space imaging of the polariton field. Here we focus on the latter method, which provides a means for direct visualization of polariton propagation (29–34). In either case, the probe pulse may be phase-matched with the polaritons, including their forward wavevector component, because the probe pulse moves through the crystal at the same speed as the excitation pulse did. However, when the polariton wave reaches the back face of the crystal and is reflected, the forward wavevector component is reversed, and the cumulative effect of the phase modulation as the probe moves through the sample is partially lost, leading to a weakening of the signal. When the polariton wave reaches the front crystal face and is reflected, the signal increases accordingly owing to the restored phase-matching.

In our experiments, imaging is achieved with frequency-doubled pulses. Owing to the shorter probe wavelength, the phase contrast generated by the traveling polariton wave is larger, and the intense scattered pump light can easily be filtered out. However, because of the difference in the group velocities of the pump and probe pulses, even the forward-propagating polariton wave is not perfectly phase-matched. Thus, a given region of the polariton profile is encountered by different parts of the probe as the latter traverses the crystal. This phenomenon becomes significant in a crystal that is thicker than $\sim 300 \mu\text{m}$, and results in a weaker and blurred signal. The deficiency can be overcome if the probe arrives at an angle (indicated in **Table 1**) that compensates for the difference in group velocities. Nevertheless, when two polariton waves propagate in opposite lateral directions, this correction will preferentially improve the imaging only in one direction and will weaken the signal in the other.

Experimental Considerations

The experimental results presented below were generated from several different laser systems and with a rather wide variety of experimental conditions. Here we do not elaborate all the experimental details for each measurement but rather point out general considerations. Some further details are provided with the discussions of individual measurements, and many more details may be found in the cited literature (29–43).

The polaritonics results reviewed here all have been obtained with Ti:sapphire femtosecond laser systems including amplifiers that operate at approximately a 1 kHz repetition rate and that produce on the order of 1 mJ energy in a pulse with a duration of roughly 50 fs. Operation in this manner is convenient because sufficient polariton amplitude (electric field levels of roughly 5 kV/cm) may be generated routinely to permit facile localized detection with a focused probe beam or spatiotemporal imaging. The polariton field pattern in a transparent crystal like LiTaO₃ or LiNbO₃ is a phase object, and various methods have been used to produce an amplitude image at the CCD camera. Usually the camera is simply moved slightly out of the image plane of a two-lens telescope, but blocking or phase shifting of part of the transmitted light also can work. Often, polariton fields in bulk crystals (with thicknesses of 0.5 mm or more) may be imaged with little or no signal averaging. Indeed, typically one can observe polariton images from an inexpensive CCD camera directly on a monitor and see polariton propagation as the probe pulse delay is varied, essentially watching a polariton “movie” as it is unfolding in the lab. This means that routine operations like the focusing of polaritons into a waveguide may be conducted with real-time visual feedback as the alignment of optical elements or the position of the host crystal is varied. Taking this a step further, it would not be difficult to implement an automated feedback loop for iterative optimization of excitation field shaping on the basis of specified parameters derived from measured images. Some measurements in our lab have been conducted using a 250-kHz repetition rate amplifier that produces pulses of 1–5-μJ energy and approximately 150-fs duration. These excitation pulse energies are still sufficient for polariton imaging, although signal averaging is required for good signal/noise levels. Recently polariton imaging has been conducted using only a femtosecond oscillator for the excitation and probe source, but the signal averaging times in this case are rather long, measured in hours (27).

The excitation fluence must be kept low enough to avoid white-light generation or other unwanted nonlinear responses such as sample damage. For a 50-fs pulse duration, that means fluences under approximately 20 mJ cm⁻². For experiments in which the polariton frequency range is approximately 1 THz or less, a longer pulse duration, roughly 150 fs, would still be essentially in the impulsive limit and would permit substantially higher excitation fluence, resulting in higher polariton amplitudes. LiNbO₃ and LiTaO₃ suffer cumulative photorefractive effects, and these may be observed readily in the images that we record. However, we have not yet noticed any impact of photorefractive damage on polariton generation. Presumably

the effect would become significant if it gave rise to substantial distortion of the excitation beam spatial profile.

All the results reviewed here were recorded with pump and probe polarizations along the optic axis, which in the images displayed is the vertical axis. Several different excitation configurations were used. In the simplest cases, the excitation light was focused to a round spot or cylindrically focused to a line at the sample. In other cases, more specialized optical elements were used to produce specified excitation patterns. The excitation light was passed through a binary phase mask, and the ± 1 diffraction orders were passed through a two-lens telescope and overlapped at the crystal to produce a spatially periodic excitation pattern; the spatial period and the number of fringes were determined by (a) the phase mask period and telescope magnification and (b) the size of the incident beam on the phase mask pattern, respectively (25, 53, 54). The excitation beam was passed through a conical prism, or axicon, and a lens to produce a circular excitation pattern, and part of this pattern was sometimes blocked to produce a semicircular or arc pattern of excitation light at the sample (32, 33). Finally, in some cases the excitation beam was incident into the spatiotemporal pulse shaper, as has been described elsewhere (36, 37). Several types of shaped excitation waveforms were used; these types were distinguished mainly by the orientation of the one spatial dimension along which the waveform was shaped relative to the crystalline optic axis (vertical throughout the discussions and images presented in this review) and to the (horizontal) direction of strongest polariton propagation. In one case, an array of spots, one above the other, was generated; each spot was 30 μm high and 150 μm wide, and the arrival times of pulses at the different spots were specified in various ways. In another case, an array of vertical lines, each 1 mm high and 30 μm wide, was constructed; the first pulse arrived at the leftmost line, the next pulse arrived at the adjacent line, and so on so that successive pulses were shifted proportionally in position and time. To extend the temporal range of this tilted pulse front waveform beyond the range achievable with the pulse shaper alone, an echelon structure consisting of four glass pieces cemented together to form a staircase structure was inserted into the beam path. In later measurements a 20-step echelon structure was used without the reconfigurable pulse shaper (55). Finally, in some cases the excitation waveform was shaped spatially in one or two dimensions but not temporally (37), and in other cases only temporal shaping was conducted (41).

Polaritonic waveguides, resonators, and other elements were fabricated through femtosecond laser machining of holes or trenches that typically were carved entirely through LiNbO_3 or LiTaO_3 host crystals that were up to 500 μm thick (38–42). For the relatively large feature sizes needed (typically tens of microns in diameter or width) high pulse energies (10–100 μJ) were used to ablate material, and repeated shots were used to drill through a crystal. The sample was mounted onto computer-controlled translational stages whose motions could be specified through a graphics file with a drawing of the features to be fabricated. Femtosecond laser machining mechanisms for this material class have been studied (56).

POLARITONICS DEVELOPMENT AND RESULTS

Early Coherent Polariton Measurements

Phonon-polaritons were characterized first through incoherent spectroscopy, particularly Raman spectroscopy conducted at various scattering angles, as early as the 1960s (20, 57–62). Coherent anti-Stokes Raman scattering (CARS) and stimulated Raman gain measurements beginning in the late 1960s and 1970s (63–72) and impulsive stimulated Raman scattering (ISRS) measurements that began in the 1980s (12, 24, 25, 73–83), including measurements on various ferroelectric crystals and measurements with spatially distinct excitation and probe regions, provided much of the ground work for polaritonics. Here we review work that began in the late 1990s with the advent of polariton spatiotemporal imaging (29, 30) and continued with the development of polariton spatiotemporal coherent control and the fabrication of integrated polaritonic structures.

Spatiotemporal Polariton Imaging

In this section we present several examples of polariton imaging (29–33) that also illustrate a variety of simple excitation configurations (without reconfigurable pulse shaping) and bulk crystal polariton properties.

Polariton propagation and reflection. **Figure 4a** shows an image of several-cycle polariton waves that were launched in LiTaO_3 by crossed, cylindrically focused excitation pulses. The image was recorded 1.3 ps following excitation, by which time the waves have moved in opposite lateral directions partly but not completely away from the excitation region and from each other. The 400-nm probe beam in this measurement was directed straight through the crystal, normal to the front and back crystal faces, although, as described above, this is not phase-matched ideally for the polariton wave propagating in either direction.

Figure 4b shows several images recorded from a 3×6 -mm LiNbO_3 crystal after excitation by a cylindrically focused excitation line source. The location of the source is evident from the image recorded while the excitation pulse was present. The response consists of two single-cycle polariton waves that propagate in opposite lateral directions. After 30 ps, the wave that was initially moving leftward is reflected by the

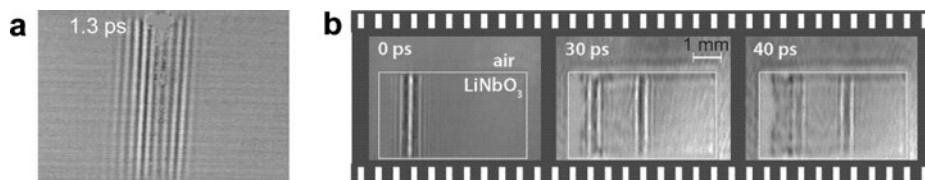


Figure 4

Imaging of spatial as well as temporal polariton evolution. (a) Multicycle and (b) single-cycle polariton waves.

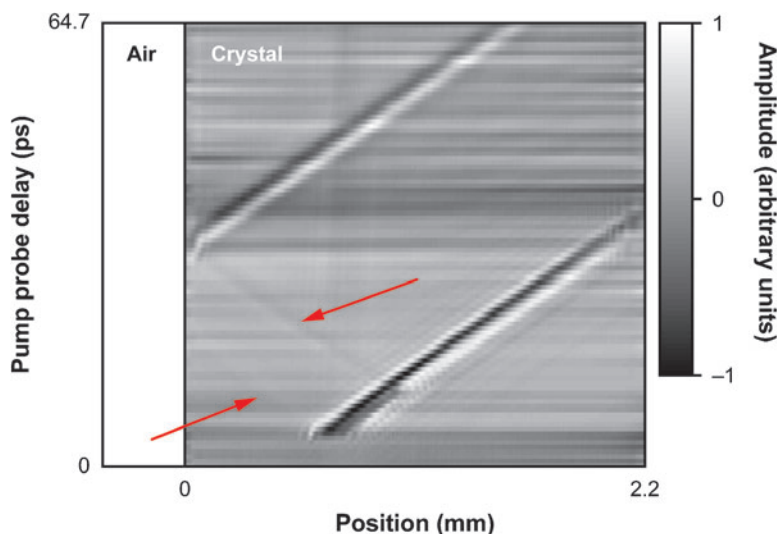


Figure 5

Space-time representation of polariton evolution. Owing to the probing angle, only polariton responses traveling to the right are strongly visible.

crystal edge and moves to the right, trailing the wave that was initially moving in that direction. Both waves have progressed farther to the right after 40 ps. In these measurements the angle between the 400-nm probe beam and the pump beam was approximately 14° , so it was properly phase-matched for right-propagating polariton waves.

This is evident in **Figure 5**, which shows an alternate, and a more complete, representation of the polariton response. For a polariton plane wave that is essentially invariant in the vertical dimension of **Figure 4b**, there is no loss of information in averaging over this dimension and reducing each two-dimensional image to a quasi-one-dimensional horizontal line. Many such images may then be displayed one above the other in time order, so the vertical dimension becomes time, and the entire spatiotemporal response may be summarized in compact form. The right-propagating polariton waves generate strong, single-cycle images as they should, but the left-propagating wave (marked by arrows in **Figure 5b**) is only dimly visible because the probe pulse is not phase-matched for its observation. In addition, there is a weak double image of the left-propagating wave because most of the signal from it is generated as the probe beam is just entering and just leaving the crystal (the signal from the bulk is more completely canceled owing to the accumulated phase mismatch), at which times it encounters the left-propagating wave at different lateral positions.

Although the images of **Figure 4** show lateral polariton propagation, as discussed above, there is a forward polariton propagation angle that is not negligible. Because of this forward angle, the angle of reflection off the left crystal face in **Figure 4b** exceeds the total internal reflection angle (which is only 11.2°), so 100% reflection occurs.

Polariton transmission. **Figure 6a** shows a case similar to that of **Figure 4b** except that there is a second crystal separated from the first by a gap of approximately $100\ \mu\text{m}$.

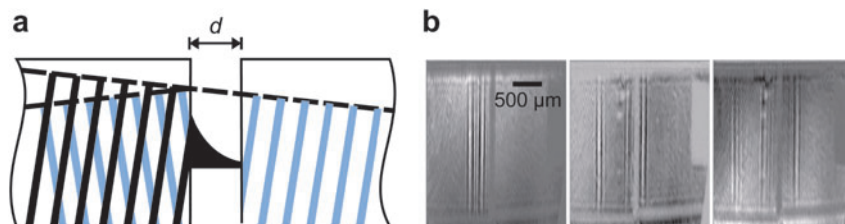


Figure 6

(a) Depending on the distance between two crystals, a substantial fraction of the amplitude may tunnel to the second crystal. (b) A polariton wave undergoes partial reflection at the side face of the left crystal and partial transmission, through evanescent coupling, into the right crystal.

Partial reflection and partial transmission from the first crystal to the second are observed. Transmission between crystals rather than total internal reflection occurs owing to evanescent coupling, or tunneling, because in air the gap is smaller than the polariton wavelength range (84). The expected exponential decay of polariton amplitude in the second crystal as a function of its separation from the first was observed.

If the side face of a LiTaO_3 or LiNbO_3 crystal is cut at an angle that matches the polariton forward propagation angle, then the polariton wave impinges on the interface at normal incidence, and a fraction of the electromagnetic part is transmitted into the air without the need for evanescent coupling into a second crystal (85). The angle dependence of the reflectivity is notable owing to the high values of the refractive index. In particular, for LiNbO_3 or LiTaO_3 the eo- or o-polarized polariton reflectivity is approximately 50% at normal incidence, decreases to zero at the Brewster angle θ_B of only $9\text{--}11^\circ$, and jumps to 100% in just another $0.1\text{--}0.2^\circ$, at which the critical angle is reached! In practice, this means that transmission out of the crystal can be increased substantially by approaching the Brewster angle, but care is required to avoid reaching the critical angle.

A Fabry-Perot-type interferometer may be realized by using two crystals with side surfaces cut at complementary angles to account for the polariton forward propagation angle, as illustrated in **Figure 7a**. For a separation between the two reflecting surfaces that exceeds the spatial extent of the phonon-polariton wavepacket in air, we expect a train of pulses to emerge from the interferometer and continue into the second crystal. The amplitude of the k th pulse in the second crystal is reduced from that of the first pulse in the first crystal by a factor $t_{ca}r_{ca}^{2(k-1)}t_{ac}$, where $t_{ij} = 2n_i/(n_i + n_j)$ and $r_{ij} = (n_i - n_j)/(n_i + n_j)$ and the subscripts (ca and ac) refer to crystal and air in the order that the pulse encounters them.

Panels *b* and *c* of **Figure 7** show measured and simulated spatial phonon-polariton amplitude distributions as a function of separation between the two crystals. The plots are similar to the condensed space-time plot shown above in that two-dimensional polariton images that do not vary in the vertical dimension have been compressed to horizontal lines. However, in this case the vertical axis is not time but crystal separation, which varies from zero (crystals touching each other) to almost 0.5 mm.

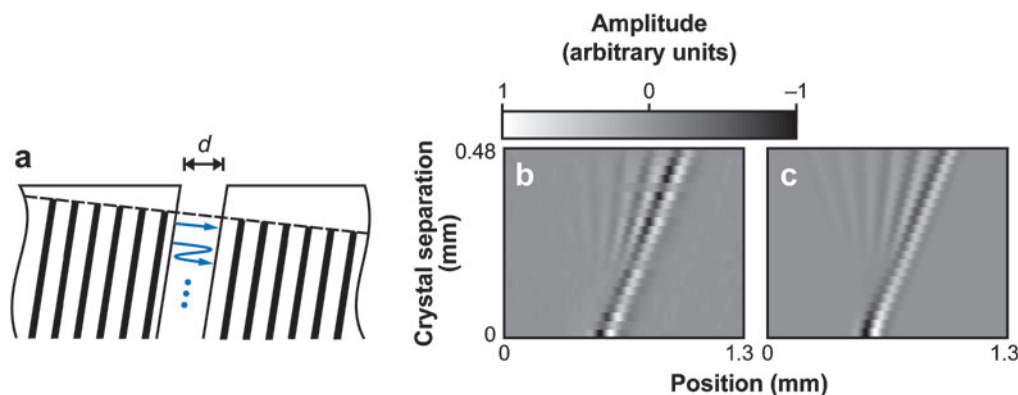


Figure 7

(a) Polaritonic Fabry-Perot interferometer. The side surfaces of the crystals are cut such that the polariton wave is incident normal to both surfaces. (b) Spatial amplitude distribution in the second crystal as a function of crystal separation d . Images were recorded at a fixed probe delay time as the first crystal position was varied. (c) Simulation.

The relative time delays and amplitudes of the successive pulses in the second crystal are reproduced well for all crystal separations.

The two-crystal configurations discussed above are useful for applications in THz spectroscopy, in which a sample may be placed or flowed between the two crystals. In such a case, the entire assembly of crystals plus sample forms a compact, integrated THz spectrometry cell with optical input and output pulses and no through-air THz propagation (86). This has recently been used for THz spectroscopy of relaxor ferroelectric crystals (87), whose extremely high dielectric constants result in very high reflection of THz radiation coming from air but significantly reduced reflection from LiTaO_3 or LiNbO_3 .

Nonplanar polariton waves. The next several examples illustrate the generation, imaging, and properties of nonplanar polariton waves in bulk crystals. **Figure 1a** shows simulations (and **Figure 9a** in the following subsection shows experimental observations) of polariton responses at various times to a round excitation spot. A single-cycle wavelet emanates outward from the excitation region, showing nearly cylindrical symmetry about an axis along the excitation laser pulse propagation direction. The strongest propagation is in the horizontal direction, perpendicular to the optic axis, which is also the polariton polarization direction and along which there is a node in the cosinusoidal amplitude distribution.

Figure 8a shows the polariton response in LiTaO_3 to a ring of excitation light produced by an axicon-lens combination (32, 33). The response collapses inward to a focus of approximately $50\ \mu\text{m}$, approximately the width of the excitation intensity distribution anywhere around the ring pattern. (A polariton response expanding outward from the excitation ring pattern does not appear in the field of view of the images.) The polariton phase front generated in this way is fully aberration-free and almost

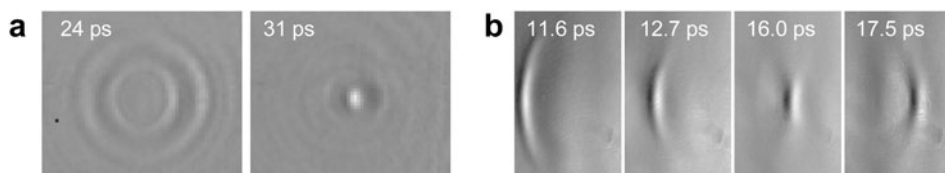


Figure 8

Polariton focusing in LiTaO_3 after excitation (a) in a circular ring pattern and (b) in an arc pattern. Spatial scales are given by the polariton speed of $50 \mu\text{m ps}^{-1}$.

perfectly circular. The initial field amplitude, however, is maximal when the generated wavefront is parallel to and minimal when it is perpendicular to the excitation and polariton polarization direction.

If part of the circular excitation pattern is blocked, an arc excitation pattern and the corresponding polariton response are generated. **Figure 8b** illustrates the results of a semicircular excitation pattern. This case is important in practice for the generation of polaritons that are focused to a desired sample location such as the mouth of a waveguide. The arc excitation pattern also allows direct observation of an effect termed the Gouy phase, in which superluminal propagation through the focus leads to phase reversal of the wavefront (32, 88).

Spatiotemporal Polariton Coherent Control

In the examples shown in the last subsection, control over polariton responses was demonstrated through useful but experimentally cumbersome means. To generate polariton responses to round, cylindrical, periodic, and ring or arc excitation patterns, different optical elements were inserted into the excitation beam path, which was then realigned. Ideally, all the adjustments could be done reconfigurably, in a fully or largely automated fashion. In addition, for the most versatile control over polariton responses, the excitation field could be tailored as a function of time as well as position. In practice, reconfigurable shaping of the excitation field as a function of time and one spatial dimension (spatiotemporal pulse shaping) (89–92) as well as temporal-only pulse shaping (93, 94) or spatial-only (in one or two spatial dimensions) beam shaping are possible. Here we illustrate some of the capabilities for coherent control over polariton responses through various forms of reconfigurable waveform shaping.

Spatiotemporal shaping. The use of the spatiotemporal pulse shaper to generate a series of point sources in a vertical line at the sample with the possibility of independent temporal control of the optical waveform at each spot yields a timed array of polariton sources, reminiscent of timed array radar sources but at GHz-THz rather than MHz frequencies. Because each of the excitation spots is a source of an outgoing polariton wavelet, the buildup of the superposed wave is a wonderful demonstration of the Huygens principle. **Figure 9** shows results obtained by imaging the output of the spatiotemporal pulse shaper onto a 2-mm-thick LiTaO_3 crystal (36).

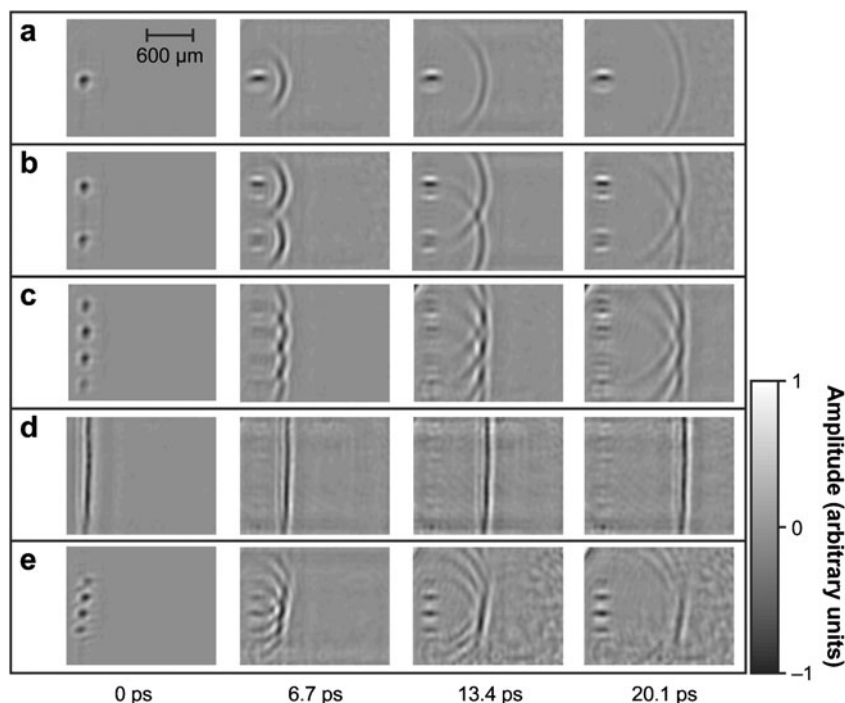


Figure 9

Phonon-polariton response to (a) one, (b) two, (c) four, and (d) nine excitation regions with all pump pulses time-coincident and (e) four excitation regions with a linear temporal sweep, the top pulse arriving first, then the second, etc. The time delay between successive snapshots is 6.7 ps. The apparent features at the excitation spot locations are due to cumulative photorefractive effects in the sample, which do not appear to affect the efficiency of phonon-polariton generation. The field of view shows only the right-propagating responses; similar responses also propagated leftward, although the probe angle was not phase-matched to detect them efficiently. Adapted from Reference 36.

From panels *a* to *d* of **Figure 9**, the number of individual excitation regions increases from 1, to 2, to 4, to 9, with a roughly proportional decrease in the separation between regions. Whereas the individual responses are apparent in **Figure 9a–c**, **Figure 9d** shows an almost perfectly planar wavefront. Up to 40 distinct excitation spots have been used to generate high-quality polariton waveforms. In **Figure 9a–d**, all the pulses arrive simultaneously at their respective spots; i.e., only a simple form of one-dimensional spatial shaping was executed. **Figure 9e** shows the polariton response to a similar spatial distribution of excitation spots imaged onto a similar LiTaO₃ crystal, but with a linear temporal sweep as introduced in the simulated data of **Figure 1a**. The coherent superposition of all the wavelets, launched at different times and at different positions, determines the spatiotemporal evolution of the propagating far-field response. The experiment is a further demonstration of the Huygens principle, the concept of controlled interferences, with a timed array of emitters.

Through the use of different linear temporal sweeps, polaritons with different amounts of tilt were generated; as a result, steered responses were sent off in different directions. Curved polariton wavefronts with different focal lengths were generated by creating parabolic excitation temporal profiles with different amounts of curvature. **Figure 1b** provides an example. In other cases, combinations of linear and parabolic temporal sweeps were applied to direct and focus the polaritons at specified times and sample locations. Although single pulses were incident on all the excitation spots in the examples shown here, multiple pulses or arbitrary temporal profiles that may or may not be similar at the different spots may be used to generate multiple-cycle or more complex wavelets and far-field superpositions.

In the above examples, the excitation waveforms were shaped temporally and spatially along the vertical (optic axis) direction of the crystalline sample. Shaping along the orthogonal direction instead allows different applications in which successive pulses may move horizontally along the crystal at light-like speeds comparable to the polariton speed, thereby manipulating the amplitude and/or phase profile of the polariton response as it propagates. Polariton amplification is particularly important for applications such as nonlinear THz spectroscopy and signal processing as well as coherent control over THz responses of materials or molecules. With a single excitation pulse, the maximum polariton amplitude that can be reached is limited by the white-light or damage threshold of the crystal. Yet the amplitude may be increased substantially beyond that limit by successive excitation events through a spatiotemporally shaped excitation waveform. In such experiments, a series of vertical lines was generated with a linear temporal sweep in the horizontal direction so that the first pulse arrived at the leftmost vertical line, the second pulse arrived at the adjacent line, and so on, with the sweep rate adjusted to match the polariton phase velocity. In this way the polariton response that propagates rightward from the first excitation line reaches the next excitation line at the same time as the corresponding excitation pulse and generates a second polariton response that superposes constructively with the first. The larger-amplitude superposition reaches the next excitation line coincident with the next excitation pulse, resulting in further constructive superposition, and so on.

Polariton amplification in this manner was demonstrated first with just two pulses that were adjusted manually (and also with two pairs of crossed pulses for amplification of multiple-cycle polariton waves) (34) and then with reconfigurable spatiotemporal pulse shaping in an early (35) and then more advanced form (36). However, because the spatiotemporally shaped waveform used for amplification is simply a sequence of spatially and temporally shifted pulses that form a tilted pulse front, it may be generated nonreconfigurably through the use of an echelon structure, and a magnification system may be used to adjust the degree of tilt to match the polariton phase velocity. **Figure 10** illustrates the experimental setup (including interferometric imaging) and the amplified polariton response in a 2-mm-thick crystal of MgO-doped stoichiometric LiNbO₃ crystal (55).

The amplified polariton response appears to develop internal structure at its highest amplitudes. This structure is not real but is an artifact owing to the polariton amplitude, which, on the basis of projection into the air and then into ZnTe in

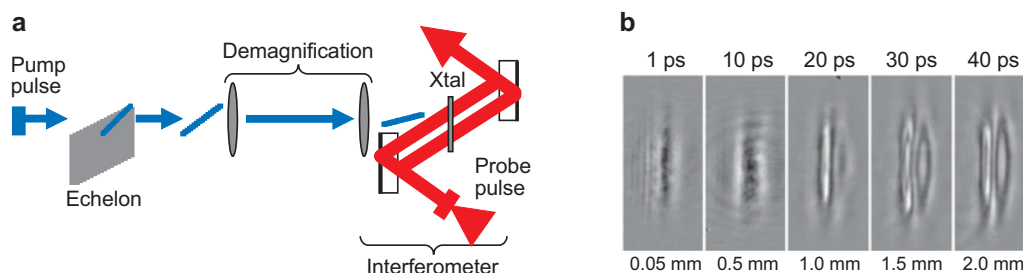


Figure 10

(a) Schematic illustration of spatiotemporal polariton amplification, using a 40-step echelon structure to generate a discrete tilted pulse front that is imaged onto the crystal to match the polariton phase velocity. Interferometric imaging permits an absolute determination of the probe phase change. (b) Images of excitation pulses (first three frames) and amplified polariton response as a function of time and position in the crystal (part b adapted from Reference 55).

which the phase shift of probing light was measured, is estimated to be approximately 50 kV/cm. The amplified single-cycle polariton response in LiNbO_3 shifts the phase of the imaging light by more than 2π at the maximum peak and null excursions. Thus, although the polariton response is a single-cycle wave, the image shows internal modulations. Still higher polariton amplitudes were generated using a grating to generate a continuous rather than a discrete tilted pulse front (85, 95, 96).

Spatial-only and temporal-only shaping. Although the combination of spatial and temporal pulse shaping provides a great deal of versatility, there are some classes of THz waveforms that are readily generated through simple two-dimensional spatial beam shaping. **Figure 11** illustrates two examples. **Figure 11a** shows an image of two multiple-cycle polariton waves that cross and interfere with each other. In **Figure 11b**, an image of two focusing polariton wavefronts, one trailing the other, is shown. The first of these foreshadows THz transient grating or four-wave mixing excitation, and

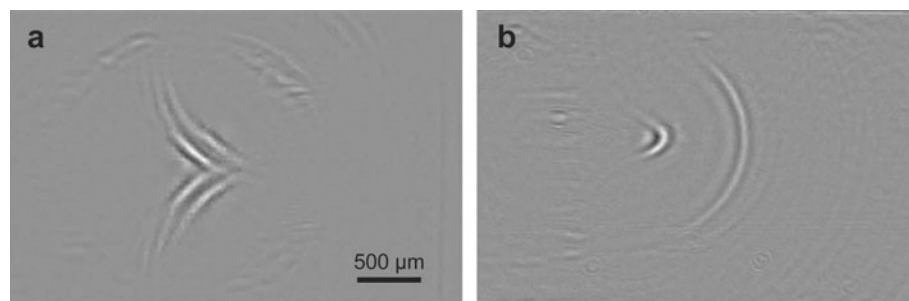


Figure 11

Polariton responses generated with reconfigurable two-dimensional spatial beam shaping. (a) Crossed polariton waveforms generated by two tilted, periodic patterns of excitation light. (b) Two focusing polariton wavefronts generated by spatially separated arc patterns of excitation light.

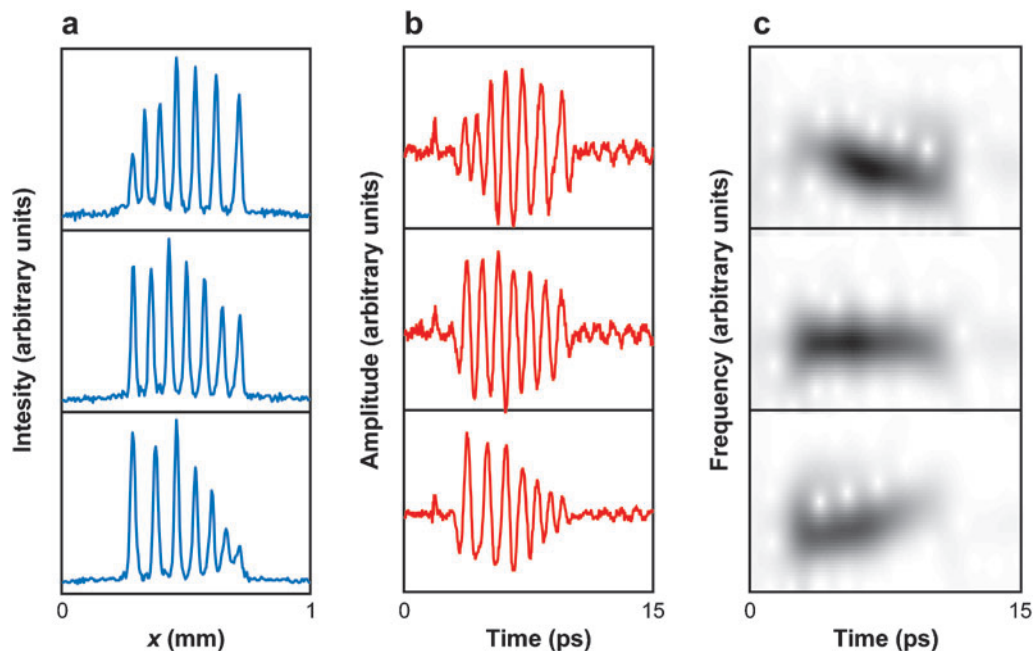


Figure 12

Unchirped and chirped THz waveforms. The excitation intensity pattern is shown in column a, the measured THz waveform in column b, and the windowed Fourier transform in column c. Adapted from Reference 37.

the second, THz pump-probe measurements in which the probe temporal delay is varied by changing the spatial separation between the two arc optical excitation features.

Simplifying still further, some important classes of waveforms that consist of a sequence of parallel plane waves may be generated through spatial beam shaping in just one dimension. In this case the optical excitation pattern simply consists of a series of parallel vertical features whose shapes and positions are adjusted to generate the specified polariton response in a form of THz typesetting (37).

Figure 12 shows examples in which patterns of excitation line sources whose spatial separations vary linearly from one side to the other, i.e., spatially chirped excitation intensity profiles, give rise to THz waveforms with corresponding temporal chirp.

Figure 13 shows compilations of one-dimensional spatial-only shaping results; panels *a* and *c* show various excitation profiles, and panels *b* and *d* show the corresponding polariton responses. Panels *a* and *b* illustrate the generation of specified THz bit patterns by appropriately patterned excitation line sources. In panels *c* and *d*, the excitation light was spatially shaped to form adjacent light and dark bands. In this case polariton generation occurs in the regions where the excitation pattern changes abruptly from light to dark. Note the complementarity between the top three and bottom three responses in **Figure 13d**. Inversion of the light and dark excitation

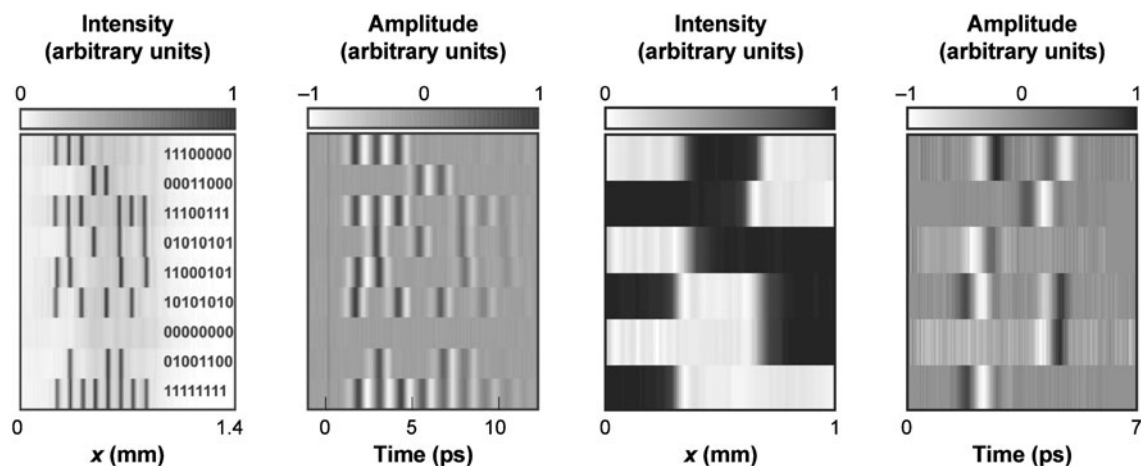


Figure 13

(*a,b*) Generation of THz waveforms representing a byte. (*a*) Intensity plot of a vertical section of the excitation profile as a function of the spatial position together with the corresponding number in binary coding. (*b*) Measured THz waveform versus probe delay time. The narrow dark line at time zero in *b* is caused by an instantaneous electronic contribution to the Kerr signal. (*c,d*) Complementary THz waveforms. (*c*) Intensity plot of a vertical section of the excitation profile as a function of the spatial position. (*d*) Measured THz waveform versus probe delay time. *a* and *b* are adapted from Reference 37.

regions leads to polariton waveforms of opposite phase. The individual polariton features take the form of single-cycle pulses with two opposite lobes of essentially equal amplitudes, whereas the polariton features generated by excitation line sources with a symmetrical (e.g., Gaussian) spatial profile like any of the isolated line sources in **Figure 13a** are spatially symmetrical as well, with one large lobe in the middle surrounded by two smaller lobes of opposite sign. These are examples of the fact that the polariton profile can be described well by the spatial derivative of the excitation intensity profile. More complex excitation spatial profiles may be used to generate THz waveforms with arbitrary amplitude and phase profiles. Temporal-only shaping of a narrowly focused excitation beam also can be used for polariton shaping, in which case the time derivative of the excitation temporal profile dictates the nature of the polariton response.

Integrated Polaritonic Structures

The examples reviewed thus far illustrate polariton generation, imaging, and control in bulk, unpatterned LiNbO_3 and LiTaO_3 crystals. Although extensive polariton control is possible through the use of various forms of excitation pulse shaping, in many cases polariton guidance and manipulation through the use of permanent sample features is desirable. Here we review the use of a variety of features such as polaritonic waveguides; resonators; reflective, diffractive, and refractive elements; and some more complex structures composed of these building blocks.

Waveguides. Before reviewing machined structures, we illustrate polariton behavior in thin LiNbO₃ films that act as planar waveguides (43). Polariton confinement in this case, in contrast to lateral confinement within laser-machined waveguides, is within the plane of the crystal. **Figure 14** shows measured (**Figure 14a,b**) and simulated (**Figure 14c,d**) images of multiple-cycle polaritons in a 10- μm -thick LiNbO₃ film that was fabricated through crystal ion slicing (97, 98). The simulations show the through-plane polariton field distribution that cannot be imaged experimentally. For polariton wavelengths that greatly exceed the film thickness, i.e., $\lambda = 87\ \mu\text{m}$, a substantial fraction of the field amplitude extends outside the film and into the air, i.e., the cladding. This results in higher phase and group velocity than for short wavelengths, e.g., $10\ \mu\text{m}$, that are confined within the film or for bulk LiNbO₃ crystals. Panels *e–h* of **Figure 14** show similar results for single-cycle polariton waves in 34- μm and 50- μm LiNbO₃ films (99). The space-time plots (**Figure 14e,g**) in this case reveal multiple waveguide modes with different phase and group velocities, as shown in the dispersion plots (**Figure 14f,h**). The higher-order modes have nodes in the crystal plane that can be viewed as arising from interference between polaritons with forward

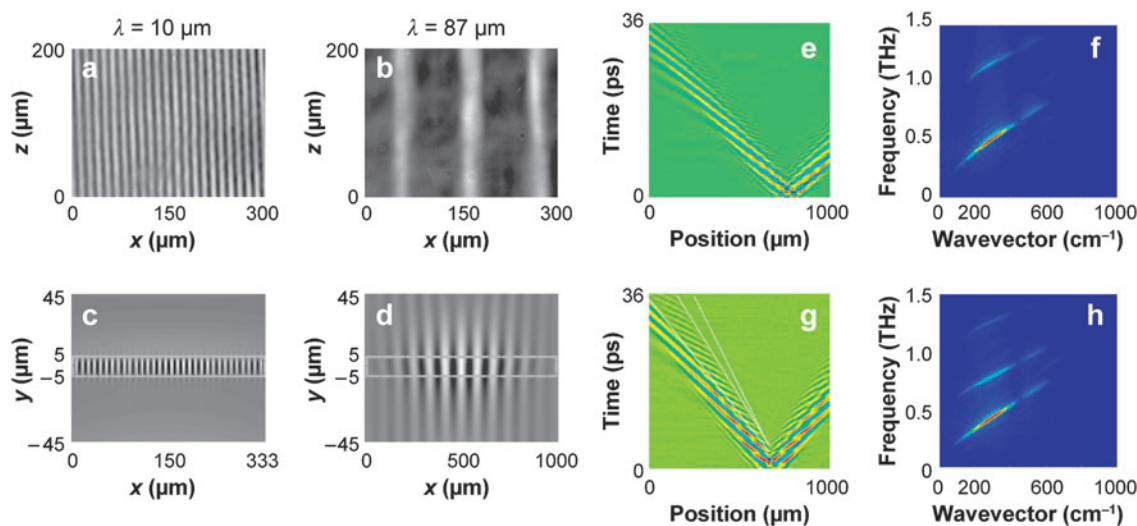


Figure 14

Polaritons in LiNbO₃ planar waveguides. (*a–d*) LiNbO₃ thickness of 10 μm . (*a,b*) Experimentally recorded images of in-plane polariton fields. (*c,d*) Simulations of through-plane fields illustrate confinement at short wavelengths (e.g., $\lambda = 10\ \mu\text{m}$) but considerable extension into the surroundings at long wavelengths (e.g., $\lambda = 87\ \mu\text{m}$). (*e,f*) LiNbO₃ thickness of 34 μm . (*g,h*) LiNbO₃ thickness of 50 μm . Space-time plots of single-cycle polariton responses (*e,g*) reveal multiple waveguide modes (separated by *white lines*) with different phase and group velocities. (*f,h*) Dispersion curves derived from Fourier transformation of space-time plots in both dimensions. Thin films are traversed sufficiently quickly by the probe pulse that the phase-matching requirement is relaxed and a normal angle of incidence can be used to view polaritons moving in both lateral directions. *a–d* are adapted from Reference 43, and *e–h* are adapted from Reference 99.

and backward wavevector components. In still-thicker films, the separation between waveguide modes becomes negligible, and the usual bulk continuum model applies well. In that limit we observe polariton propagation with intermittent, temporally distinct reflections off the back and front crystal faces.

We turn now to structures that were fabricated through femtosecond laser machining (38, 42). **Figure 15** shows images from a linear waveguide, a Mach-Zehnder interferometer, and a Y-coupler in 500- μm -thick LiNbO_3 crystals. The structures are defined by unmachined material between air trenches that were carved completely through the crystal. **Figure 1c** shows the Y-coupler. The structures appear blurry in the images that show polaritons because the CCD camera was moved out of the image plane for high-contrast phase imaging. Panels *a* and *b* of **Figure 15** show single-cycle polaritons that have been focused into the mouth of a waveguide using a nearly

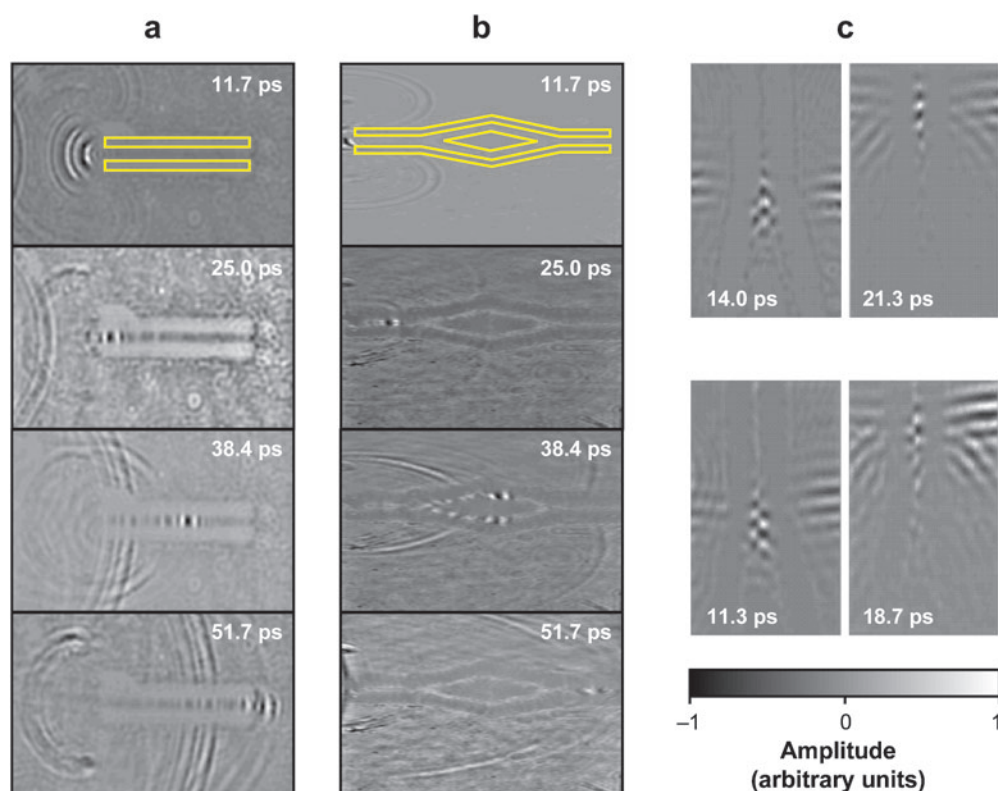


Figure 15

Polariton propagation in waveguide structures carved into a 500- μm -thick LiNbO_3 crystal. (*a*) Single-cycle wave focused into a 200- μm -wide, 1.7-mm-long waveguide. (*b*) Single-cycle wave focused into waveguide interferometer. Waveguide channels are 170 μm wide, and the region of split waves is 1 mm long. (*c*) Close-up. Fourier-filtered images of multiple-cycle waves in a Y-coupler with 170- μm -wide channels. See **Figure 1c**. In-phase or out-of-phase superposition of input waves results in a symmetric or asymmetric output channel signal, respectively.

semicircular excitation pattern illustrated above. The entrance, propagation, and exit of the polaritons can be seen clearly, and within the waveguide nearly perfectly planar wavefronts are observed. As in the planar waveguide case, the phase and group velocities may be determined and readily compared with those in the unpatterned bulk crystal. In some cases, signals in different waveguide modes that separate after some propagation owing to their different group velocities may be observed. The splitting and recombination within the interferometer could be exploited for THz signal processing or spectroscopic applications. **Figure 1c** shows polariton propagation through the Y-coupler. In that case, a multiple-cycle plane wave was incident on the two input channels, and the waves that entered were superposed upon reaching the output channel. **Figure 15c** shows close-up images of two cases in which the multicycle wave was incident on the structure at different angles so that the two input channel waves would superpose in phase or out of phase. The results are output signals in symmetric or asymmetric waveguide modes, respectively.

Resonators. Next we illustrate polaritonic resonators, another class of structures that are important in their own right and are building blocks for more complex functionalities. **Figure 16** shows a single image of a several-cycle wave in a 300- μm -wide resonator that was fabricated through removal of two approximately 500 $\mu\text{m} \times 600 \mu\text{m}$ square regions of crystalline material from either side (40). Fundamental and overtone modes—including details such as the forward polariton wavevector component, the bevel angle of the resonator walls, and planar waveguide effects

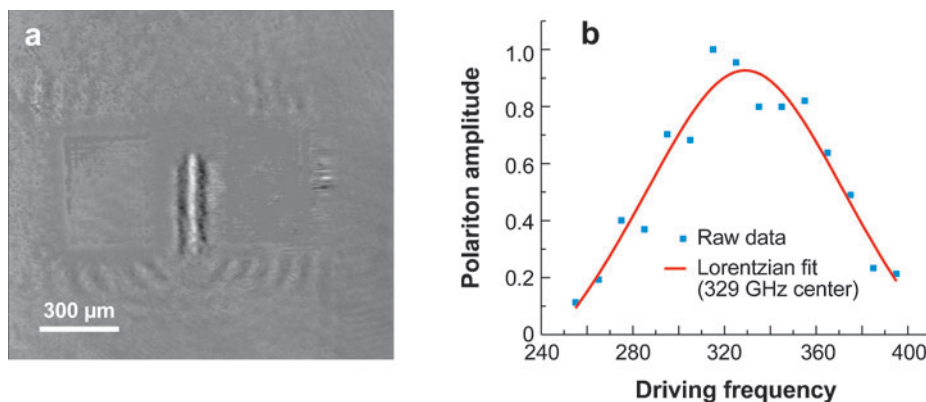


Figure 16

(a) Polariton amplitude distribution in a 300- μm -wide LiNbO_3 resonator driven in an overtone mode by crossed excitation pulses. By crossing two excitation beams to generate standing-wave polaritons of 80- μm wavelength, a selected overtone mode of the resonator is excited. Leakage out of the sides of the resonator as well as the response confined within it can be observed. (b) Maximum polariton amplitude achieved after excitation at the middle of the resonator by a cylindrically focused line of light that contained a sequence of seven evenly spaced excitation pulses with a roughly Gaussian temporal envelope. The highest amplitude is achieved when the pulse repetition rate matches the fundamental resonator frequency of 325 GHz. *b* is adapted from Reference 41.

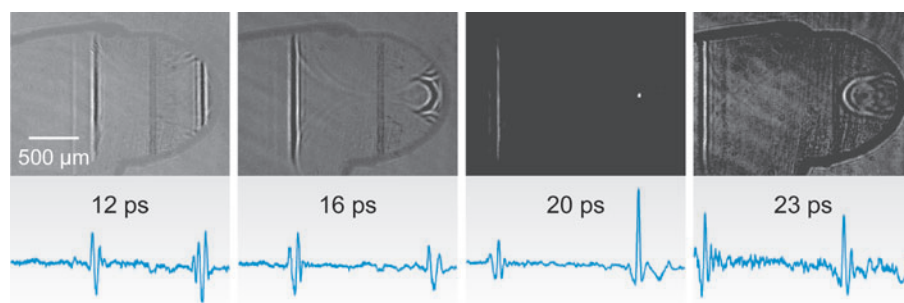


Figure 17

The polariton wavepacket moving to the right is focused by the curved reflector in a LiNbO_3 crystal.

in the 250- μm -thick LiNbO_3 crystal—were observed and analyzed. In general, the performance (i.e., the Q-factor) of the resonator is enhanced by the forward polariton wavevector component, which leads to total internal reflection at the boundaries.

Unlike in an unpatterned crystal, polariton amplification in a resonator structure may be executed with temporal-only shaping (41). **Figure 16b** shows the response of the same resonator illustrated above to a timed sequence of evenly spaced excitation pulses, as a function of the repetition rate of the pulses within the sequence.

Focusing reflector. **Figure 17** shows images of a polariton plane wavepacket in LiNbO_3 that is focused by a curved reflecting structure. The fabricated structure is part of an ellipse whose major and minor axes are in the ratio of the LiNbO_3 refractive index components for extraordinary and ordinary polarizations, respectively. Unlike focusing by a circular or arc excitation pattern, the use of a focusing reflector may be combined with polariton amplification to achieve particularly high amplitudes. This has been demonstrated recently, and nonlinear LiNbO_3 lattice vibrational responses have been observed at the focus (100).

Diffraction elements. We turn now to structures involving diffraction and interference (39). The structure of primary practical interest is a diffraction grating, formed as a series of evenly spaced features that reflect polariton wave components that are incident on them. **Figure 18a** shows the grating structure that we discuss.

The array of elements results in interference among the reflected and transmitted components from an incident wave, as we see shortly. Because the buildup of the diffracted waves in the far field may be illustrated elegantly starting with the reflections at each region of the wave in the near field, we start by showing the response to a single element, then to two elements, then to the array of ten elements that forms the grating structure. **Figure 18b** shows a wave that has been reflected by a single machined feature that is far wider than the wavelength components of the polariton wavepacket but whose edges are sharp relative to the wavelengths. In this case, diffraction off of each edge results in curved wavefronts that are well separated by the planar reflection from the middle of the structure. Next we consider diffraction by a

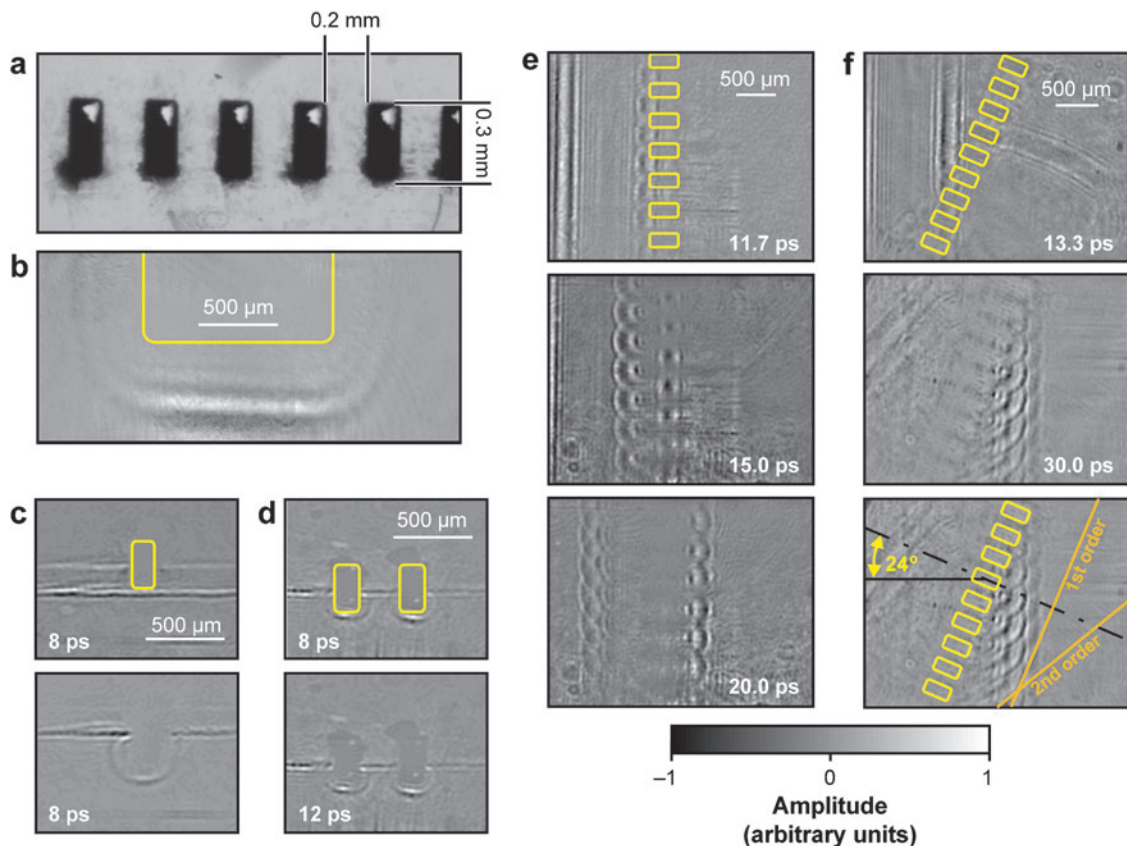


Figure 18

Diffraction elements in 0.5-mm-thick LiNbO_3 . (a) Microscope image of laser-machined grating structure. (b) Polariton wavepacket reflected by a single element wider than those of the grating. The incident wavepacket was moving from bottom to top in *b–d*. (c) Polariton wavepacket reflected by a single element identical to those of the grating. (d) Polariton diffraction by two elements identical to those of the grating. (e) Polariton diffraction upon zero-degree incidence on the grating. The incident wavepacket was moving from left to right in *e* and *f*. (f) Polariton diffraction upon 25° incidence on the grating. The expanded view at 30 ps reveals first- and second-order diffraction phase fronts (adapted from Reference 39).

single element with the same dimensions as those of the grating. **Figure 18c** shows that the reflected wavefront is almost perfectly circular, with no central planar component. In the forward direction, the diffraction pattern from an obstacle is observed. **Figure 18d** shows the results from two features with the same dimensions as those of the grating. As expected, in reflection almost perfectly circular wavefronts originate at both structures to form a double-slit interference pattern when their amplitudes overlap spatially. The interference pattern from two wires is observed at later times in transmission. **Figure 18e** shows a sequence of snapshots of the polariton spatial amplitude as the wavepacket intercepts the grating structure at normal incidence.

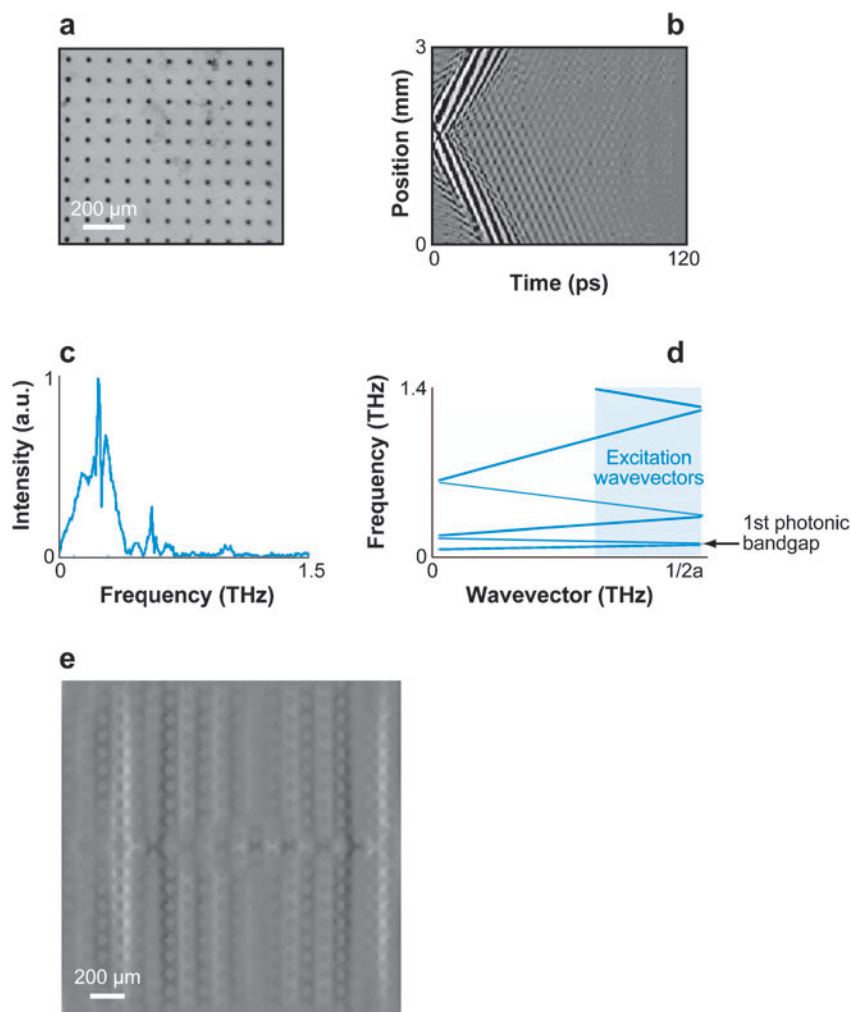


Figure 19

(a) Polaritonic bandgap crystal. (b) Space-time plot of polariton response. (c) Fourier transform of *b* at a selected crystal location. (d) Theoretical polaritonic bandgap dispersion curve. (e) Image of polariton field distribution within the structure, temporally Fourier filtered from 285–325 GHz, spatially around the allowed wavevectors of the crystal, and with signal artifacts from the air holes removed. *a–d* are adapted from Reference 99.

Approximately 15 ps after the excitation, one part of the wavepacket is reflected, and the other part is located within the short waveguides between the grating lines. As time goes on, the interferences in the transmitted and reflected wavefronts become more and more pronounced. **Figure 18e** shows images for a geometry in which the polariton wavepacket intercepts the grating at a nonzero angle. Owing to the imaging geometry and the polarization of the imaging beam, the transmitted signal is far more pronounced than the reflection. At a delay of approximately 30 ps almost all the wavepacket has passed the grating structure, and the buildup of the interference structure is clearly visible. The central wavelength of the incident polariton wavepacket is approximately 0.15 mm. The angle of incidence in **Figure 18e** is 25°. For a grating constant of 0.34 mm one would expect the first-order diffraction to appear close to

the grating normal and the second-order diffraction at approximately an angle of 27° , as indicated by straight lines in **Figure 18e** and in excellent agreement with the observed diffracted wavefronts. With a grating/curved mirror combination, it should be possible to realize a compact, all-integrated phonon-polariton spectrometer.

Polaritonic bandgap structure. We close this section with an illustration of a somewhat more complex structure: a photonic, or polaritonic, bandgap material consisting of a two-dimensional array of air holes that form a square lattice, as shown in **Figure 19** (99). Broadband phonon-polaritons with a center wavelength of twice the lattice periodicity were generated within the structure. A condensed display of the resulting propagation is shown in **Figure 19b**, with the Fourier transform of the response measured at a selected crystal location slightly offset from the excitation region shown in **Figure 19c**. The polariton wavevector range is indicated on the right-hand edge of the theoretically calculated dispersion diagram shown in **Figure 19d**. Although a single line of excitation light produces a broadband polariton wavepacket in an unpatterned crystal, the bandgap structure strongly filters the response, resulting in a narrowed bandwidth, as is evident by the multiple cycles revealed in **Figure 19b**. The lowest six branches of the photonic dispersion curve (**Figure 19d**) are evident in the Fourier transform; the lower-frequency mode of each pair has higher signal strength owing to its field localization primarily in the crystalline material (where it is observable in our images) and its counterpart's localization primarily in the air regions.

Figure 19e shows an image of the field within the bandgap structure. The polaritonics platform may provide a unique optics testbed for bandgap materials and other complex structures.

CLOSING REMARKS

We present here a comprehensive review of THz polaritonics methods and results achieved in recent years. THz generation and shaping, propagation, control, guidance, and imaging are all supported in the integrated polaritonics solid-state platform.

Several current efforts and trends are moving polaritonics beyond the developmental stage and into the phase of applications in THz signal processing as well as THz spectroscopy and coherent control. Recent technical advances include the demonstration of coupled polaritonic waveguides and the introduction of the excitation light at an angle such that purely lateral polariton propagation in the crystal plane takes place. This excitation angle also enables pseudo-phase-matched polariton amplification by pump light that is multiply reflected off the back and front crystal faces (55).

Although this review deals exclusively with polariton behavior in the linear response regime, nonlinear spectroscopy and coherent control of THz-frequency material responses—including low-frequency electronic resonances (atomic and molecular Rydberg coherences) (101–104), intersubband transitions in quantum wells and quantum dots (105–107), lattice vibrations, and molecular and ionic motions in liquids and partially disordered systems—present unique possibilities. Nonlinear lattice

vibrational responses in LiNbO₃ have recently been driven by amplified polariton waves that were focused and crossed by a curved reflector like that illustrated above (100). This represents the first nonlinear THz spectroscopy measurement conducted using the polaritonics platform. Hybrid polaritonic structures with integrated quantum well and quantum dot constituents are currently under exploration for polaritonic coherent control over intersubband coherences. Shaped polariton fields of sufficient amplitude may enable coherent control over collective material structure, including ferroelectric or other crystal domain orientation and phase transitions. Wide-ranging applications of polaritonics in linear and nonlinear response regimes await demonstration.

ACKNOWLEDGMENTS

This work was supported in part by NSF Grant No. CHE-0212375, NSF MRSEC Program, Grant No. DMR-0213282, ARO Grant No. DAAD 10-01-10-674, ONR Grants No. N00014-06-1-0463 and N00014-06-1-0459, and Cambridge-MIT Institute Project No. CMI-001.

LITERATURE CITED

1. Beard MC, Turner GM, Schmuttenmaer CA. 2002. Terahertz spectroscopy. *J. Phys. Chem. B* 106:7146–59
2. Mittleman D. 2003. Sensing with terahertz radiation. Berlin: Springer-Verlag
3. Han PY, Zhang X-C. 2001. Free-space coherent broadband terahertz time-domain spectroscopy? *Meas. Sci. Technol.* 12:1747–56
4. Ferguson B, Zhang XC. 2002. Materials for terahertz science and technology. *Nature Mater.* 1:26–33
5. Davies AG, Linfield EH, Johnston MB. 2002. The development of terahertz sources and their applications. *Phys. Med. Biol.* 47:3679–89
6. Schmuttenmaer CA. 2004. Exploring dynamics in the far-infrared with terahertz spectroscopy. *Chem. Rev.* 104:1759–79
7. Sakai K, ed. 2005. *Terahertz Optoelectronics*. Berlin: Springer
8. Smith PR, Auston DH, Nuss MC. 1988. Subpicosecond photoconducting dipole antennas. *IEEE J. Quantum Electron.* 24:255–60
9. Fattinger C, Grischkowsky D. 1989. Terahertz beams. *Appl. Phys. Lett.* 54:490–92
10. van Exeter M, Grischkowsky DR. 1990. Characterization of an optoelectronic terahertz beam system. *IEEE Trans. Microw. Theory Tech.* 38:1684–91
11. You D, Jones RR, Bucksbaum PH, Dykaar DR. 1993. Generation of high-power subsingle-cycle 500-fs electromagnetic pulses. *Opt. Lett.* 18:290–92
12. Auston DH, Nuss MC. 1988. Electrooptical generation and detection of femtosecond electrical transients. *IEEE J. Quantum Electron.* 24:184–97
13. Hu BB, Zhang XC, Auston DH, Smith PR. 1990. Free-space radiation from electrooptic crystals. *Appl. Phys. Lett.* 56:506–8

14. Carrig TJ, Rodriguez G, Clement TS, Taylor AJ, Stewart KR. 1995. Scaling of terahertz radiation via optical rectification in electrooptic crystals. *Appl. Phys. Lett.* 66:121–23
15. Nahata A, Welington AS, Heinz TF. 1996. A wideband coherent terahertz spectroscopy system using optical rectification and electro-optic sampling. *Appl. Phys. Lett.* 69:2321–23
16. Bonvalet A, Joffre M, Martin JL, Migus A. 1995. Generation of ultrabroadband pulses in the mid-infrared by optical rectification of 15 fs light pulses at a 100 MHz repetition rate. *Appl. Phys. Lett.* 67:2907–9
17. Lee YS, Meade T, Perlin V, Winful H, Norris TB, Galvanauskas A. 2000. Generation of narrow-band terahertz generation via optical rectification of femtosecond pulses in periodically poled lithium niobate. *Appl. Phys. Lett.* 76:2505–7
18. Cook DJ, Hochstrasser RM. 2000. Intense terahertz pulses by four-wave rectification in air. *Opt. Lett.* 25:1210–12
19. Bartel T, Gaal P, Reimann K, Woerner M, Elsaesser T. 2005. Generation of single-cycle THz transients with high electric-field amplitudes. *Opt. Lett.* 30:2805–7
20. Barker AS, Loudon R. 1972. Response functions in the theory of Raman scattering by vibrational and polariton modes in dielectric crystals. *Rev. Mod. Phys.* 44:18–47
21. Born M, Huang K. 2000. *Dynamical Theory of Crystal Lattices*. Oxford, UK: Oxford Univ. Press. Reissue
22. Yan YX, Gamble EB Jr, Nelson KA. 1985. Impulsive stimulated scattering: general importance in femtosecond laser pulse interactions with matter, and spectroscopic applications. *J. Chem. Phys.* 83:5391–99
23. Dhar L, Rogers JA, Nelson KA. 1994. Time-resolved vibrational spectroscopy in the impulsive limit. *Chem. Rev.* 94:157–93
24. Dougherty T-P, Wiederrecht GP, Nelson KA. 1992. Impulsive stimulated Raman scattering experiments in the polariton regime. *J. Opt. Soc. Am. B* 9:2179–89
25. Crimmins TF, Stoyanov NS, Nelson KA. 2002. Heterodyned impulsive stimulated Raman scattering of phonon-polaritons in LiTaO_3 and LiNbO_3 . *J. Chem. Phys.* 117:2882–96
26. Kleinman DA, Auston DH. 1984. Theory of electrooptic shock radiation in nonlinear optic media. *IEEE J. Quantum Electron.* 20:964–70
27. Wahlstrand JK, Merlin R. 2003. Cherenkov radiation emitted by ultrafast laser pulses and the generation of coherent polaritons. *Phys. Rev. B* 68:054301
28. Lines ME, Glass AM. 2001. *Principles and Applications of Ferroelectrics and Related Materials*. New York: Oxford Univ. Press
29. Koehl RM, Adachi S, Nelson KA. 1999. Real-space polariton wave packet imaging. *J. Chem. Phys.* 110:1317–20
30. Koehl RM, Adachi S, Nelson KA. 1999. Direct visualization of collective wavepacket dynamics. *J. Phys. Chem. A* 103:10260–67
31. Koehl RM, Crimmins TF, Nelson KA. 2001. Lattice vibrations that move at the speed of light: How to excite them, how to monitor them, and how to image them before they get away. In *Ultrafast Infrared and Raman Spectroscopy*, ed. MD Fayer, pp. 513–39. New York: Marcel Dekker

32. Feurer T, Stoyanov NS, Ward DW, Nelson KA. 2002. Direct visualization of the Gouy phase by focusing phonon-polaritons. *Phys. Rev. Lett.* 88:257402
33. Stoyanov NS, Ward DW, Feurer T, Nelson KA. 2002. Direct visualization of phonon-polariton focusing and amplitude enhancement. *J. Chem. Phys.* 117:2897-901
34. Koehl RM, Nelson KA. 2001. Coherent optical control over collective vibrations traveling at light-like speeds. *J. Chem. Phys.* 114:1443-46
35. Koehl RM, Nelson KA. 2001. Terahertz polaritonics: automated spatiotemporal control over propagating lattice waves. *Chem. Phys.* 267:151-59
36. Feurer T, Vaughan JC, Nelson KA. 2003. Spatiotemporal coherent control of lattice vibrational waves. *Science* 299:374-77
37. Feurer T, Vaughan JC, Hornung T, Nelson KA. 2004. Typesetting of THz waveforms. *Opt. Lett.* 29:1802-4
38. Stoyanov NS, Ward DW, Feurer T, Nelson KA. 2002. Terahertz polariton propagation in patterned materials. *Nature Mater.* 725:95-98
39. Stoyanov NS, Feurer T, Ward DW, Nelson KA. 2002. Integrated diffractive THz elements. *Appl. Phys. Lett.* 82:674-76
40. Stoyanov NS, Feurer T, Ward DW, Statz ER, Nelson KA. 2004. Direct visualization of a polariton resonator in the THz regime. *Opt. Exp.* 12:2387-96
41. Ward DW, Beers JD, Feurer T, Statz E, Stoyanov NS, Nelson KA. 2004. Coherent control of phonon-polaritons in a THz resonator fabricated with femtosecond laser machining. *Opt. Lett.* 29:2671-73
42. Ward DW, Statz ER, Nelson KA. 2007. Fabrication of polaritonic structures in LiNbO₃ and LiTaO₃ using femtosecond laser machining. *Appl. Phys. A* 86:49-54
43. Ward DW, Statz ER, Nelson KA, Roth RM, Osgood RM. 2005. Terahertz wave generation and propagation in thin film lithium niobate produced by crystal ion slicing. *Appl. Phys. Lett.* 86:022908
44. Hobden MV, Warner J. 1966. The temperature dependence of the refractive indices of pure lithium niobate. *Phys. Lett.* 22:243-44
45. Bruner A, Eger D, Oron MB, Blau P, Katz M, Ruschkin S. 2003. Temperature-dependent Sellmeier equation for the refractive index of stoichiometric lithium tantalate. *Opt. Lett.* 28:194-96
46. Barker AS, Loudon R. 1967. Dielectric properties and optical phonons in LiNbO₃. *Phys. Rev.* 158:433-45
47. Barker AS Jr, Ballman AA, Ditzenberger JA. 1970. Infrared study of the lattice vibrations in LiTaO₃. *Phys. Rev. B* 2:4233-39
48. Huard S. 1997. *Polarization of Light*. Paris: Wiley & Masson
49. Taflov A, Hagness SC. 2000. *Computational Electrodynamics: The Finite-Difference Time-Domain Method*. Boston: Artec House. 2nd ed.
50. Ward DW. 2005. *Polaritonics: an intermediate regime between electronics and photonics*. PhD thesis. Massachusetts Institute of Technology
51. Nye JF. 1985. *Physical Properties of Crystals*. Oxford: Oxford Univ. Press
52. Ruhman S, Kohler B, Joly AG, Nelson KA. 1988. Coherent molecular vibrational motion observed in the time domain through impulsive stimulated Raman scattering. *IEEE J. Quantum Electron.* 24:460-69

53. Maznev AA, Nelson KA. 1998. How to make femtosecond pulses overlap. *Opt. Lett.* 23:1378–80
54. Maznev AA, Nelson KA, Rogers JA. 1998. Optical heterodyne detection of laser-induced gratings. *Opt. Lett.* 23:1319–21
55. Yeh KL, Hornung T, Vaughan JC, Nelson KA. 2007. Terahertz amplification in high-dielectric materials. In *Ultrafast Phenomena XV*, ed. P Corkum, DM Jonas, RJD Miller, AM Weiner. Berlin: Springer. In press
56. Deshpande DC, Malshe AP, Stach EA, Radmilovic V, Alexander D, et al. 2005. Investigation of femtosecond laser assisted nano and microscale modifications in lithium niobate. *J. Appl. Phys.* 97:074316
57. Henry CH, Hopfield JJ. 1965. Raman scattering from polaritons. *Phys. Rev. Lett.* 15:964–66
58. Porto SPS, Tell B, Damen TC. 1966. Near-forward Raman scattering in zinc oxide. *Phys. Rev. Lett.* 16:450–52
59. Scott JF, Cheesman LE, Porto SPS. 1967. Polariton spectrum of α -quartz. *Phys. Rev.* 162:834–40
60. Puthoff HE, Pantell RH, Huth BG, Chacon MA. 1968. Near-forward Raman scattering in LiNbO_3 . *J. Appl. Phys.* 39:2144–46
61. Pinczuk A, Burstein E, Ushioda S. 1969. Raman scattering by polaritons in tetragonal BaTiO_3 . *Solid State Commun.* 7:139–42
62. Penna AF, Chaves A, Andrade P da R, Porto SPS. 1976. Light scattering by lithium tantalate at room temperature. *Phys. Rev. B* 13:4907–17
63. Kurtz SK, Giordmaine JA. 1969. Stimulated Raman scattering by polaritons. *Phys. Rev. Lett.* 22:192–95
64. Gelbwachs J, Pantell RH, Puthoff HE, Yarborough JM. 1969. A tunable stimulated Raman oscillator. *Appl. Phys. Lett.* 14:258–62
65. Yarborough JM, Sussman SS, Puthoff HE, Pantell RH, Johnson BC. 1969. Tunable optical emission from LiNbO_3 without a resonator. *Appl. Phys. Lett.* 15:102–5
66. Johnson BC, Puthoff HE, SooHoo J, Sussman SS. 1971. Power and linewidth of tunable stimulated far-infrared emission in LiNbO_3 . *Appl. Phys. Lett.* 18:181–83
67. Gale GM, Vallee FG, Flytzanis C. 1986. Propagation and dephasing of picosecond phonon polariton pulses in ammonium chloride. *Phys. Rev. Lett.* 57:1867–70
68. Valle F, Flytzanis C. 1992. Temporal and spatial evolution of picosecond phonon-polariton pulses in crystals. *Phys. Rev. B* 46:13799–812
69. Schwarz UT, Maier M. 1996. Frequency dependence of phonon-polariton damping in lithium niobate. *Phys. Rev. B* 53:5074–77
70. Schwarz UT, Maier M. 1998. Damping mechanisms of phonon polaritons, exploited by stimulated Raman gain measurements. *Phys. Rev. B* 58:766–75
71. Qiu T, Maier M. 1997. Long-distance propagation and damping of low-frequency phonon polaritons in LiNbO_3 . *Phys. Rev. B* 56:R5717–20
72. Qiu T, Tillert T, Maier M. 1995. Tunable, kilowatt, picosecond far-infrared pulse generation in LiNbO_3 . *Opt. Commun.* 119:149–53
73. Auston DH, Cheung KP, Valdmanis JA, Kleinman DA. 1984. Cherenkov radiation from femtosecond optical pulses in electro-optic media. *Phys. Rev. Lett.* 53:1555–58

74. Auston DH, Cheung KP. 1985. Coherent time-domain far-infrared spectroscopy. *J. Opt. Soc. Am. B* 2:606–12
75. Etchepare J, Grillon G, Antonetti A, Loulergue JC, Fontana MD, Kugel GE. 1990. Third-order nonlinear susceptibilities and polariton modes in PbTiO_3 obtained by temporal measurements. *Phys. Rev. B* 41:12362–65
76. Kien DP, Loulergue JC, Etchepare J. 1993. Nonlinear response to polariton waves driven in perovskites by femtosecond pulses. *Opt. Commun.* 101:53–59
77. Albert O, Duijser M, Loulergue JC, Etchepare J. 1996. Time-resolved nonlinearities from nonsymmetric polar phonons in PbTiO_3 and KNbO_3 perovskites. *J. Opt. Soc. B* 13:29–33
78. Dougherty TP, Wiederrecht GP, Nelson KA, Garrett MH, Jenssen HP, Warde C. 1992. Femtosecond resolution of soft mode dynamics in structural phase transitions. *Science* 258:770–74
79. Dougherty TP, Wiederrecht GP, Nelson KA, Garrett MH, Jenssen HP, Warde C. 1994. Femtosecond time-resolved spectroscopy of soft modes in structural phase transitions of perovskites. *Phys. Rev. B* 50:8996–9019
80. Wiederrecht GP, Dougherty TP, Dhar L, Nelson KA, Leaird DE, Weiner AM. 1995. Explanation of anomalous polariton dynamics in LiTaO_3 . *Phys. Rev. B* 51:916–31
81. Planken PCM, Noordam LD, Kennis JTM, Legendijk A. 1992. Femtosecond time-resolved study of the generation and propagation of phonon polaritons in LiNbO_3 . *Phys. Rev. B* 45:7106–14
82. Grenier P, Houde D, Jandl S, Boatner LA. 1993. Soft-mode studies in $\text{KTa}_{0.93}\text{Nb}_{0.07}\text{O}_3$ with use of the time-resolved third-order optical susceptibility χ^3 . *Phys. Rev. B* 47:1–4
83. Grenier P, Houde D, Jandl S, Boatner LA. 1994. Measurement of the soft polariton in $\text{KTa}_{0.93}\text{Nb}_{0.07}\text{O}_3$ by time-resolved four-wave mixing. *Phys. Rev. B* 50:16295–308
84. Carey JJ, Zawadzka J, Jaroszynski DA, Wynne K. 2000. Noncausal time response in frustrated total internal reflection. *Phys. Rev. Lett.* 84:1431–34
85. Stepanov AG, Hebling J, Kuhl J. 2003. Efficient generation of subpicosecond terahertz radiation by phase-matched optical rectification using ultrashort laser pulses with tilted pulse fronts. *Appl. Phys. Lett.* 83:3000–2
86. Crimmins TF, Gleason MJ, Ward DW, Nelson KA. 2001. A simple terahertz spectrometer. In *Ultrafast Phenomena XII*, ed. T Elsaesser, S Mukamel, MM Murnane, NF Scherer, 66:221–23. Berlin: Springer-Verlag
87. Paxton BJ. 2006. *Development of phonon-polariton THz spectroscopy, and the investigation of relaxor ferroelectrics*. PhD thesis. Massachusetts Institute of Technology
88. Gouy LG. 1890. Sur une propriété nouvelle des ondes lumineuses. *Acad. Sci. Paris* 110:1251–53
89. Feurer T, Vaughan JC, Koehl RM, Nelson KA. 2002. Multidimensional control of femtosecond pulses using a programmable liquid crystal matrix. *Opt. Lett.* 27:652–54
90. Vaughan JC, Feurer T, Nelson KA. 2002. Automated two-dimensional femtosecond pulse shaping. *J. Opt. Soc. Am. B* 19:2489–95

91. Vaughan JC, Feurer T, Nelson KA. 2003. Automated spatiotemporal diffraction of ultrashort laser pulses. *Opt. Lett.* 28:2408–10
92. Vaughan JC, Hornung T, Feurer T, Nelson KA. 2005. Diffraction-based femtosecond pulse shaping with a 2D SLM. *Opt. Lett.* 30:323–25
93. Weiner AM, Heritage JP, Kirschner EM. 1988. High-resolution femtosecond pulse shaping. *J. Opt. Soc. Am. B* 5:1563–72
94. Weiner AM. 2000. Femtosecond pulse shaping using spatial light modulators. *Rev. Sci. Instrum.* 71:1929–60
95. Hebling J, Stepanov AG, Almasi G, Bartal B, Kuhl J. 2004. Tunable THz pulse generation by optical rectification of ultrashort laser pulses with tilted pulse fronts. *Appl. Phys. B* 78:593–99
96. Stepanov AG, Kuhl J, Kozma IZ, Riedle E, Almasi G, Hebling J. 2005. Scaling up the energy of THz pulses created by optical rectification. *Opt. Exp.* 13:5762–68
97. Radojevic AM, Levy M, Osgood JRM, Kumar A, Bakhru H, et al. 1999. Large etch-selectivity enhancement in the epitaxial liftoff of single-crystal LiNbO₃ films. *Appl. Phys. Lett.* 74:3197–99
98. Ramadan TA, Levy M, Osgood JRM. 2000. Electro-optic modulation in crystal-ion-sliced z-cut LiNbO₃ thin films. *Appl. Phys. Lett.* 76:1407–9
99. Statz ER, Ward DW, Nelson KA. 2007. Phonon-polariton excitation in ferroelectric slab waveguides and photonic crystals. In *Ultrafast Phenomena XV*, ed. P Corkum, DM Jonas, RJD Miller, AM Weiner. Berlin: Springer. In press
100. Hornung T, Yeh KL, Nelson KA. 2007. Terahertz nonlinear response in lithium niobate. In *Ultrafast Phenomena XV*, ed. P Corkum, DM Jonas, RJD Miller, AM Weiner. Berlin: Springer. In press
101. Jones R, You D, Bucksbaum PH. 1993. Ionization of Rydberg atoms by subpicosecond half-cycle electromagnetic pulses. *Phys. Rev. Lett.* 70:1236–39
102. Schumacher DW, Hoogenraad JH, Pinkos D, Bucksbaum PH. 1995. Programmable cesium Rydberg wave packets. *Phys. Rev. A* 52:4719–26
103. Raman C, Decamp MF, Bucksbaum PH. 1997. Redistribution of atomic Rydberg states by tunable narrow band picosecond far-infrared pulses. *Opt. Exp.* 1:186–96
104. Wesdorp C, Robicheaux F, Noordam LD. 2001. Displacing Rydberg electrons: the mono-cycle nature of half-cycle pulses. *Phys. Rev. Lett.* 87:083001
105. Kersting R, Bratschitsch R, Strasser G, Unterrainer K, Heyman JN. 2000. Sampling a terahertz dipole transition with subcycle time resolution. *Opt. Lett.* 25:272–74
106. Batista AA, Citrin DS. 2004. Rabi flopping in a two-level system with a time-dependent energy renormalization: intersubband transitions in quantum wells. *Phys. Rev. Lett.* 92:127404
107. Carter SG, Birkedal V, Wang CS, Coldren LA, Maslov AV, et al. 2005. Quantum coherence in an optical modulator. *Science* 310:651–53



Contents

MATERIALS CHARACTERIZATION

Low-Temperature Degradation of Zirconia and Implications for Biomedical Implants <i>Jérôme Chevalier, Laurent Gremillard, and Sylvain Deville</i>	1
Single-Molecule Micromanipulation Techniques <i>K. C. Neuman, T. Lionnet, and J.-F. Allemand</i>	33
Spin-Polarized Scanning Tunneling Microscopy of Magnetic Structures and Antiferromagnetic Thin Films <i>Wulf Wulfbekel and Jürgen Kirschner</i>	69
Microscale Characterization of Mechanical Properties <i>K. J. Hemker and W. N. Sharpe, Jr.</i>	93
Three-Dimensional Atom-Probe Tomography: Advances and Applications <i>David N. Seidman</i>	127
The Study of Nanovolumes of Amorphous Materials Using Electron Scattering <i>David J. H. Cockayne</i>	159
Nanoscale Electromechanics of Ferroelectric and Biological Systems: A New Dimension in Scanning Probe Microscopy <i>Sergei V. Kalinin, Brian J. Rodriguez, Stephen Jesse, Edgar Karapetian, Boris Mirman, Eugene A. Eliseev, and Anna N. Morozovska</i>	189
AFM and Acoustics: Fast, Quantitative Nanomechanical Mapping <i>Bryan D. Huey</i>	351
Electron Holography: Applications to Materials Questions <i>Hannes Lichte, Petr Formanek, Andreas Lenk, Martin Linck, Christopher Matzeck, Michael Lehmann, and Paul Simon</i>	539
Three-Dimensional Characterization of Microstructure by Electron Back-Scatter Diffraction <i>Anthony D. Rollett, S.-B. Lee, R. Campman, and G.S. Robrer</i>	627

Atom Probe Tomography of Electronic Materials <i>Thomas F. Kelly, David J. Larson, Keith Thompson, Roger L. Alvis, Joseph H. Bunton, Jesse D. Olson, and Brian P. Gorman</i>	681
Electron Holography: Phase Imaging with Nanometer Resolution <i>Martha R. McCartney and David J. Smith</i>	729
FERROELECTRICS AND RELATED MATERIALS, David R. Clarke and Venkatraman Gopalan, Guest Editors	
Atomic-Level Simulation of Ferroelectricity in Oxides: Current Status and Opportunities <i>Simon R. Phillpot, Susan B. Sinnott, and Aravind Asthagiri</i>	239
Ferroelectric Domain Breakdown <i>Michel Molotskii, Yossi Rosenwaks, and Gil Rosenman</i>	271
Local Structure of Ferroelectric Materials <i>T. Egami</i>	297
Terahertz Polaritonics <i>T. Feurer, Nikolay S. Stoyanov, David W. Ward, Joshua C. Vaughan, Eric R. Statz, and Keith A. Nelson</i>	317
Spiral Magnets as Magnetoelectrics <i>T. Kimura</i>	387
Universal Domain Wall Dynamics in Disordered Ferroic Materials <i>W. Kleemann</i>	415
Defect–Domain Wall Interactions in Trigonal Ferroelectrics <i>Venkatraman Gopalan, Völkmar Dierolf, and David A. Scrymgeour</i>	449
Influence of Electric Field and Mechanical Stresses on the Fracture of Ferroelectrics <i>Gerold A. Schneider</i>	491
Strain Tuning of Ferroelectric Thin Films <i>Darrell G. Schlom, Long-Qing Chen, Chang-Beom Eom, Karin M. Rabe, Stephen K. Streiffer, and Jean-Marc Triscone</i>	589
Ferroelectric Epitaxial Thin Films for Integrated Optics <i>Bruce W. Wessels</i>	659

Index

Cumulative Index of Contributing Authors, Volumes 33–37	769
---	-----

Errata

An online log of corrections to *Annual Review of Materials Research* chapters (if any, 1997 to the present) may be found at <http://matsci.annualreviews.org/errata.shtml>